processes

MDPI

Article

Predictable Performance Control for Trajectory Tracking and Obstacle Avoidance of Differential-Drive Mobile Robots

Ruijuan Liu [1], Bing Zhang [2,3] and Zhuo-Yun Nie [3,*]

[1] School of Mathematics and Statistics, Xiamen University of Technology, Xiamen 361024, China; liuruijuan0313@163.com
[2] School of Agriculture, Nanyang Agricultural Vocational College, Nanyang 473000, China; zhangbing101@foxmail.com
[3] College of Information Science and Engineering, Huaqiao University, Xiamen 361021, China
* Correspondence: yezhuyun2004@sina.com

Abstract

This paper presents a unified framework for trajectory tracking and static obstacle avoidance of differential-drive mobile robots. A nominal exact-decoupling controller achieves pure exponential longitudinal convergence and globally avoids angular singularities via a stereographic projection; its cascade structure is proved globally asymptotically stable, and a time-scale separation analysis yields an explicit lateral settling-time constant, enabling prescribed convergence design. To handle obstacles, an artificial potential field (APF) correction is superimposed in a structure-preserving manner: the cancellation term responsible for longitudinal decoupling is retained, so the longitudinal error dynamics remain decoupled and are only additively perturbed during avoidance. The perturbed closed loop is modelled as a cascade driven by bounded inputs, and a bounded-input bounded-state (BIBS) analysis guarantees that tracking errors stay bounded during avoidance and recover exponentially with the nominal time constants once the influence zone is left. Quantitative error bounds and a recovery-time estimate enable an explicit safety–performance trade-off. Simulations on circular and figure-eight trajectories with single and multiple static obstacles confirm the predicted recovery behaviour and reduce the total integral squared error (ISE) by factors of 7.4 and 20 relative to a CBF-QP safety filter, with lateral recovery about twice as fast as that of a Kanayama controller augmented by APF.

Keywords: nonholonomic mobile robot; trajectory tracking; obstacle avoidance; artificial potential field; bounded-input bounded-state stability; cascade systems

Check for updates

Academic Editors: Raouf Fareh and Mohammad H. Rahman

Received: 25 August 2026
Revised: 23 September 2026
Accepted: 28 September 2026
Published: 5 November 2026

Copyright: © 2026 by the authors. Licensee MDPI, Basel, Switzerland. This article is an open access article distributed under the terms and conditions of the Creative Commons Attribution (CC BY) license.

1. Introduction

Differential-drive wheeled mobile robots (WMRs) are fundamental platforms in autonomous navigation, logistics, and service robotics [1]. Their nonholonomic constraint $\dot{x}\sin\theta - \dot{y}\cos\theta = 0$ and underactuation (two inputs, three degrees of freedom) make trajectory tracking their predominant control paradigm: Brockett's condition [2] rules out asymptotic stabilisation by continuous time-invariant feedback, whereas trajectory tracking is feasible and has been extensively studied [3]. A feasible reference trajectory provides persistent excitation and maintains controllability [4,5]. Beyond stability, engineering applications demand predictable dynamic responses (e.g., settling time, overshoot) to facilitate gain tuning and system integration. However, the intrinsic coupling among longitudinal, lateral, and heading errors makes it extremely challenging to prescribe the convergence performance of individual error channels independently.

The seminal work by Kanayama et al. [6] proposed a Lyapunov-based tracking controller that guarantees local asymptotic stability under nonzero reference velocity. It suffers from three inherent limitations: the error dynamics remain coupled, preventing independent tuning of settling times; the heading error is confined to $(-\pi, \pi)$, causing unwinding problems near $\pm\pi$ [7]; and the relationship between gains and convergence rates is implicit. Subsequent research has sought to overcome these deficiencies. Backstepping and cascade designs [8–10] provide systematic Lyapunov constructions but still entangle the three error channels. Sliding mode control (SMC) [11,12] enhances robustness yet introduces chattering and lacks explicit gain-to-performance mapping. Meanwhile, observer-based designs have enabled trajectory tracking under general time-varying references with partial state measurements [13], yet the three error channels remain coupled, leaving independent per-channel performance tuning out of reach. Prescribed performance control (PPC) [14,15] confines errors within decaying envelopes, but the transformation from performance functions to controller gains remains indirect. Recent developments have extended the PPC framework to path following of nonholonomic vehicles [16] and to angle-constrained adaptive formation control [17]; nevertheless, these designs prescribe transient error envelopes rather than an explicit gain-to-settling-time mapping for the individual error channels.

When operating in cluttered environments, trajectory tracking must be integrated with obstacle avoidance. The artificial potential field (APF) method [18,19] is widely used for its simplicity, but a direct superposition of repulsive forces onto a coupled tracking controller generally destroys any nominal decoupling property and may lead to unpredictable recovery. Control barrier functions (CBFs) [20,21] offer a rigorous safety certificate, but when applied as a minimal-intervention quadratic-program filter to a highly coupled nonlinear tracker, they can severely degrade tracking accuracy, as will be demonstrated in this paper. Recent advances have addressed the feasibility and conservatism issues in CBF-QP formulations by introducing hierarchical frameworks that prioritise safety while preserving performance objectives [22]. Integrated planning-and-control frameworks that combine prescribed-time tracking with collision-free navigation have likewise been pursued [23]. Across these lines of work, however, safety enforcement and explicit per-channel performance prediction are realised by separate mechanisms; preserving the nominal gain-to-settling-time map throughout the avoidance maneuver itself has, to the best of our knowledge, not been explicitly pursued.

To fill this gap, this paper proposes a novel continuous state-feedback controller for trajectory tracking of differential-drive WMRs, together with a unified obstacle-aware extension. The core innovations are threefold. First, a nonlinear feedforward term $y_e\omega$ in the linear velocity command exactly cancels the coupling in $\dot{x}_e$, leading to $\dot{x}_e = -k_x x_e$—pure exponential convergence with a user-assigned rate, completely independent of lateral and heading transients. Second, the stereographic projection $\Theta = \tan(\theta_e/2)$ maps the heading error onto $\mathbb{R}$, eliminating the topological singularity and enabling a smooth, globally defined control law without switching. Third, we extend the nominal controller to obstacle avoidance by superimposing structure-preserving APF corrections: the actual (corrected) angular velocity is fed into the $y_e\omega$ cancellation term, preserving exact longitudinal decoupling even during aggressive avoidance maneuvers.

Furthermore, a quantitative performance analysis is carried out. Through linearisation and singular perturbation, an explicit lateral slow-mode time constant $\tau_y = k_\theta/(4k_y v_r^2)$ is derived under the separation condition $k_\theta \gg 4\sqrt{k_y}v_r$. This allows the designer to prescribe the settling time of the lateral error directly. For the obstacle-aware case, conservative bounds on peak tracking deviations are derived as functions of the APF parameters, enabling a safety–performance trade-off without extensive simulations.

The closed-loop nominal system is proved globally asymptotically stable using cascade theory and LaSalle's invariance principle. Under bounded APF corrections, the perturbed cascade is shown to be bounded-input bounded-state (BIBS) stable, and the tracking errors recover exponentially with the nominal time constants after the obstacle is cleared. Extensive simulations on circular and figure-eight trajectories confirm that the proposed method outperforms the Kanayama controller, a self-tuning baseline, and a CBF-QP safety filter in terms of tracking accuracy and predictable, verifiable recovery while maintaining collision-free operation.

The remainder of this paper is organised as follows. Section 2 presents the robot kinematic model, the error dynamics, the stereographic projection, and the obstacle representation. Section 3 details the nominal predictable-performance tracking controller and its stability analysis, proceeding in three stages—exact longitudinal decoupling, cascade stability, and time-scale separation—whose Lyapunov function is deliberately reused in Section 4. Section 4 extends the design to obstacle avoidance via structure-preserving APF corrections and analyzes the boundedness and recovery properties, with the nominal cascade recovered exactly whenever the corrections vanish. Section 5 validates the theoretical results through numerical simulations. Finally, Section 6 concludes the paper.

2. Problem Formulation and Preliminaries

2.1. Robot Kinematic Model and Tracking Error Dynamics

Consider a differential-drive mobile robot with pose $\mathbf{q} = [x, y, \theta]^\mathsf{T}$ and kinematic model [1,6,7],

$$\dot{x} = v\cos\theta, \quad \dot{y} = v\sin\theta, \quad \dot{\theta} = \omega, \tag{1}$$

subject to the nonholonomic constraint $\dot{x}\sin\theta - \dot{y}\cos\theta = 0$. The control inputs are the linear and angular velocities $v(t), \omega(t)$.

A virtual reference robot generates the desired trajectory $\mathbf{q}_r = [x_r, y_r, \theta_r]^\mathsf{T}$ via

$$\dot{x}_r = v_r\cos\theta_r, \quad \dot{y}_r = v_r\sin\theta_r, \quad \dot{\theta}_r = \omega_r, \tag{2}$$

with reference velocities $v_r(t), \omega_r(t)$. The tracking error in the body frame is defined as

$$\mathbf{e} = [x_e, y_e, \theta_e]^\mathsf{T} = \begin{bmatrix} \cos\theta & \sin\theta & 0 \\ -\sin\theta & \cos\theta & 0 \\ 0 & 0 & 1 \end{bmatrix} (\mathbf{q}_r - \mathbf{q}). \tag{3}$$

As illustrated in Figure 1, differentiating (3) and using (1)–(2) gives the error dynamics

$$\dot{x}_e = y_e\omega - v + v_r\cos\theta_e, \quad \dot{y}_e = -x_e\omega + v_r\sin\theta_e, \quad \dot{\theta}_e = \omega_r - \omega, \tag{4}$$

defined on $\mathbb{R}^2 \times (-\pi, \pi)$.

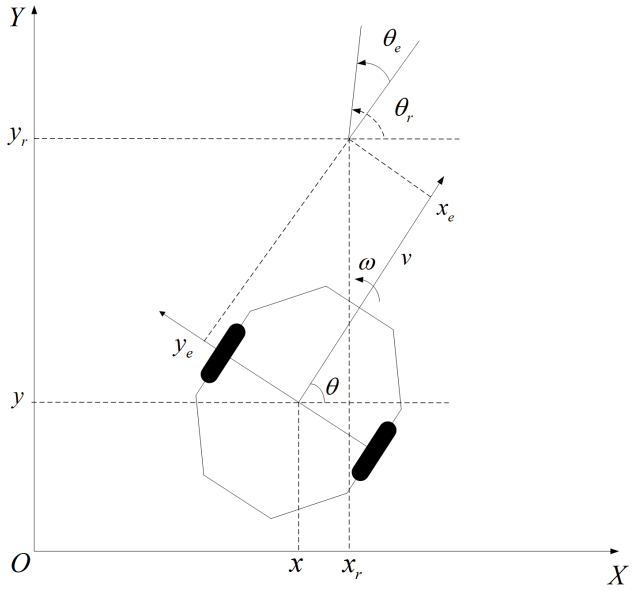


Figure 1. Kinematic model of the differential-drive mobile robot.

2.2. Stereographic Projection

To handle the angular error globally on $(-\pi, \pi)$ and avoid singularities when θ_e approaches $\pm\pi$, we employ the stereographic projection [24]

$$\Theta = \tan\frac{\theta_e}{2}, \tag{5}$$

which is a smooth bijection from $(-\pi, \pi)$ onto $\mathbb{R}$. The inverse mapping is $\theta_e = 2\arctan\Theta$. Using the identities

$$\sin\theta_e = \frac{2\Theta}{1+\Theta^2}, \qquad \cos\theta_e = \frac{1-\Theta^2}{1+\Theta^2}, \tag{6}$$

the error dynamics (4) can be rewritten in the transformed coordinates as

$$\begin{aligned} \dot{x}_e &= y_e\omega - v + v_r\frac{1-\Theta^2}{1+\Theta^2}, \\ \dot{y}_e &= -x_e\omega + v_r\frac{2\Theta}{1+\Theta^2}, \\ \dot{\Theta} &= \frac{1+\Theta^2}{2}(\omega_r - \omega). \end{aligned} \tag{7}$$

2.3. Obstacle Representation and APF Basics

The robot must also avoid N static obstacles at $\mathbf{o}_i = [x_{oi}, y_{oi}]^\mathsf{T}$. Let $d_i = \|\mathbf{p} - \mathbf{o}_i\|$ with $\mathbf{p} = [x, y]^\mathsf{T}$ be the Euclidean distance, and $\phi_i = \text{atan2}(y_{oi} - y,\ x_{oi} - x) - \theta$ be the relative bearing in the body frame. Following [18,19], we assign a repulsive APF

$$U_i(d_i) = \begin{cases} \dfrac{\eta}{2}\Big(\dfrac{1}{d_i} - \dfrac{1}{d_0}\Big)^2, & d_i < d_0, \\ 0, & d_i \geq d_0, \end{cases} \tag{8}$$

with gain $\eta > 0$ and influence radius $d_0 > 0$. The repulsive force $\mathbf{F}_i = -\nabla U_i$ acts along the direction from the obstacle to the robot:

$$\mathbf{F}_i = \begin{cases} \eta\Big(\dfrac{1}{d_i} - \dfrac{1}{d_0}\Big)\dfrac{1}{d_i^2}\,\hat{\mathbf{r}}_i, & d_i < d_0, \\ \mathbf{0}, & d_i \geq d_0, \end{cases} \tag{9}$$

where $\hat{\mathbf{r}}_i = (\mathbf{p} - \mathbf{o}_i)/d_i$. Decomposing $\mathbf{F}_i$ into the robot body frame yields longitudinal and lateral components, which will be used as avoidance velocity corrections in Section 4.

2.4. Control Objectives

The control objectives are twofold:

(i) Nominal tracking: Design v and ω such that $\mathbf{e}(t)$ converges asymptotically to zero, with exactly exponential longitudinal error and predictable lateral convergence via an explicit time constant.

(ii) Obstacle-aware control: In the presence of obstacles, the robot must avoid collisions with bounded tracking errors, and recover to the nominal convergence rates after the maneuver, with quantifiable worst-case deviations.

2.5. Assumptions

We impose the following assumptions, which are standard for trajectory tracking of wheeled robots and are extended to accommodate the obstacle avoidance scenario.

Assumption 1. *The reference velocities $v_r(t)$ and $\omega_r(t)$ are piecewise continuous and bounded. Let $v_{\max} := \sup_{t\geq 0} v_r(t) < \infty$ and $\omega_{\max} := \sup_{t\geq 0} |\omega_r(t)| < \infty$. The reference linear velocity is nonnegative: $v_r(t) \geq 0$ for all $t \geq 0$.*

Assumption 2. *There exists a constant $v_{\min} > 0$ such that $v_r(t) \geq v_{\min}$ for all $t \geq 0$. This condition ensures that on the set where the Lyapunov derivative vanishes we can conclude $y_e = 0$ (see Lemma 1). It is satisfied by all non-stopping reference trajectories.*

Assumption 3. *For the purpose of rigorous stability analysis, the reference velocities v_r and ω_r are assumed constant (autonomous case). We emphasise that ω_r may be any constant and, in particular, need not vanish: it is exactly cancelled by the feedforward term of the control law (10), and it enters the subsequent analysis only through the bound $\omega_{\max}$ of Assumption 1; no result of this paper requires $\omega_r = 0$ (see also Section 3.3). The case of slowly varying reference trajectories is examined numerically in Section 5; the extension of the theoretical analysis to genuinely time-varying references remains an open problem beyond the scope of this paper.*

Assumption 4. *The initial heading error satisfies $|\theta_e(0)| < \pi$. Consequently, the stereographic projection $\Theta = \tan(\theta_e/2)$ is well-defined initially. For the nominal closed loop, the invariance of the domain $|\theta_e| < \pi$ is proved in Remark 1 of Section 3; in the obstacle-aware case, the controller and APF parameters are selected so as to maintain this invariance throughout the avoidance maneuver, which serves as a standing condition in the analysis of Section 4 and is verified a posteriori in Section 5.*

Assumption 5. *The obstacle positions $\mathbf{o}_i$ are static and known to the robot within its sensing range. The robot does not start inside any obstacle influence zone; i.e., $d_i(0) \geq d_0$ for all i. Moreover, the obstacles are sufficiently spaced so that influence zones do not overlap with the reference trajectory for more than a finite time interval. This ensures that the obstacle-induced perturbations are temporary. In addition, the controller parameters and the influence radius d_0 are selected such that the distance to every active obstacle remains strictly positive during the entire avoidance maneuver; i.e., there exists $d_{\min} > 0$ such that $d_i(t) \geq d_{\min}$ for all i and for all t belonging to the (finite) avoidance interval. This standard design requirement for APF-based schemes is verified a posteriori in the simulations in Section 5.*

3. Nominal Predictable-Performance Tracking Controller

3.1. Controller Design and Closed-Loop Cascade

Starting from the transformed error dynamics (7), we propose the continuous state-feedback law

$$\begin{aligned} v &= y_e\omega + v_r\frac{1-\Theta^2}{1+\Theta^2} + k_x x_e, \\ \omega &= \omega_r + \frac{2k_\theta\Theta}{1+\Theta^2} + \frac{4k_y v_r y_e}{(1+\Theta^2)^2}, \end{aligned} \tag{10}$$

where $k_x, k_\theta, k_y > 0$ are constant gains and $\Theta = \tan(\theta_e/2)$. In the original heading coordinates, the control law reads $v = y_e\omega + v_r\cos\theta_e + k_x x_e$ and $\omega = \omega_r + k_\theta \sin\theta_e + 4k_y v_r y_e \cos^4(\theta_e/2)$. The term $y_e\omega$ in the linear velocity command is the structural key: it cancels the coupling $y_e\omega$ present in $\dot{x}_e$, leading to exact longitudinal decoupling without any approximation.

Substituting (10) into (7) gives the closed-loop error dynamics

$$\dot{x}_e = -k_x x_e, \tag{11}$$

$$\dot{y}_e = -x_e\omega + v_r\frac{2\Theta}{1+\Theta^2}, \tag{12}$$

$$\dot{\Theta} = -k_\theta\Theta - \frac{2k_y v_r y_e}{1+\Theta^2}. \tag{13}$$

Define $z = [y_e, \Theta]^\top$. The system takes the cascade form

$$\dot{x}_e = -k_x x_e, \qquad \dot{z} = f(z) + g(z)x_e, \tag{14}$$

with

$$f(z) = \begin{bmatrix} v_r\dfrac{2\Theta}{1+\Theta^2} \\ -k_\theta\Theta - \dfrac{2k_y v_r y_e}{1+\Theta^2} \end{bmatrix}, \qquad g(z) = \begin{bmatrix} -\omega(z) \\ 0 \end{bmatrix},$$

where $\omega(z)$ denotes the angular velocity command (10) expressed in terms of z.

3.2. Global Asymptotic Stability

We first analyze the nominal z-subsystem obtained by setting $x_e \equiv 0$ in (12)–(13):

$$\dot{y}_e = v_r\frac{2\Theta}{1+\Theta^2}, \qquad \dot{\Theta} = -k_\theta\Theta - \frac{2k_y v_r y_e}{1+\Theta^2}. \tag{15}$$

Lemma 1 (Stability of the nominal z-subsystem)**.** *For system (15) with constant $v_r > 0$ and gains $k_\theta, k_y > 0$, the origin $(y_e, \Theta) = (0,0)$ is globally asymptotically stable and locally exponentially stable.*

Proof. Consider the Lyapunov function candidate

$$V_0(y_e, \Theta) = \frac{1}{2}y_e^2 + \frac{1}{2k_y}\Theta^2,$$

which is positive definite and radially unbounded. Its time derivative along (15) is

$$\begin{aligned} \dot{V}_0 &= y_e\dot{y}_e + \frac{1}{k_y}\Theta\dot{\Theta} \\ &= y_e\Big(v_r\frac{2\Theta}{1+\Theta^2}\Big) + \frac{1}{k_y}\Theta\Big(-k_\theta\Theta - \frac{2k_y v_r y_e}{1+\Theta^2}\Big) \\ &= \frac{2v_r y_e\Theta}{1+\Theta^2} - \frac{k_\theta}{k_y}\Theta^2 - \frac{2v_r y_e\Theta}{1+\Theta^2} = -\frac{k_\theta}{k_y}\Theta^2 \le 0. \end{aligned}$$

Hence, V_0 is nonincreasing and the origin is stable. The set where $\dot{V}_0 = 0$ is $S = \{(y_e, \Theta) : \Theta = 0\}$. On S, $\Theta \equiv 0$ and therefore $\dot{\Theta} \equiv 0$. From the second equation of (15) we obtain

$$0 = -k_\theta \cdot 0 - \frac{2k_y v_r y_e}{1+0} = -2k_y v_r y_e,$$

which forces $y_e = 0$ because $k_y > 0$ and $v_r \geq v_{\min} > 0$ by Assumption 2. Thus the largest invariant set contained in S is the origin. By LaSalle's invariance principle [25], every trajectory of (15) converges to $(0,0)$ as $t \to \infty$. Because V_0 is radially unbounded, the origin is globally asymptotically stable. Local exponential stability follows from linearisation, which yields the characteristic polynomial $\lambda^2 + k_\theta \lambda + 4k_y v_r^2 = 0$ with roots having strictly negative real parts. □

Theorem 1 (Global asymptotic stability of the nominal system)**.** *Consider the closed-loop system* (11)–(13) *under Assumptions 1–4. If the reference linear velocity satisfies* $v_r(t) \geq v_{\min} > 0$ *for all* $t \geq 0$ *and is constant, then the equilibrium* $(x_e, y_e, \Theta) = (0,0,0)$ *is globally asymptotically stable. Moreover, the longitudinal error converges exponentially:*

$$x_e(t) = x_e(0)\, e^{-k_x t}. \tag{16}$$

Proof. From (11) we have $\dot{x}_e = -k_x x_e$; hence, $x_e(t)$ is globally exponentially stable (GES) and uniformly bounded by $|x_e(0)|$. In particular, $x_e(t) = x_e(0)e^{-k_x t}$, which is precisely (16). The remaining proof is organised in three steps: Step 1 establishes an explicit uniform bound of the (y_e, Θ)-subsystem that remains valid during the whole transient in which x_e decays, thereby making the effect of the transient coupling rigorous; Step 2 proves $(y_e, \Theta) \to (0,0)$ via Barbalat's lemma; Step 3 assembles the two results.

Step 1 (uniform boundedness during the decay of x_e): Consider $V_0(y_e, \Theta) = \frac{1}{2}y_e^2 + \frac{1}{2k_y}\Theta^2$. Along the full closed loop (12)–(13), the terms $\pm\frac{2v_r y_e \Theta}{1+\Theta^2}$ cancel exactly and

$$\dot{V}_0 \;=\; -\frac{k_\theta}{k_y}\Theta^2 \;-\; x_e\, \omega(z)\, y_e,$$

where $\omega(z) = \omega_r + \frac{2k_\theta \Theta}{1+\Theta^2} + \frac{4k_y v_r y_e}{(1+\Theta^2)^2}$ is the angular velocity command in (10). The coupling term is bounded globally, without any a priori boundedness assumption on Θ. Using $\left|\frac{2\Theta}{1+\Theta^2}\right| \leq 1$, $\frac{1}{(1+\Theta^2)^2} \leq 1$, $|y_e| \leq \sqrt{2V_0}$, and $|x_e(t)| = |x_e(0)|e^{-k_x t}$,

$$\dot{V}_0 \;\leq\; |x_e(0)|\, e^{-k_x t}\Big[\sqrt{2}\,(\omega_{\max} + k_\theta)\, V_0^{1/2} + 8k_y v_r\, V_0\Big],$$

with $\omega_{\max} = \sup_{t\geq 0}|\omega_r(t)|$ from Assumption 1. Set $W = \sqrt{V_0}$ and, for technical convenience, $W_\varepsilon = \sqrt{V_0 + \varepsilon^2}$ with $\varepsilon > 0$, which is continuously differentiable along the trajectories. Since $V_0^{1/2} \leq W_\varepsilon$ and $V_0 \leq W_\varepsilon^2$,

$$\dot{W}_\varepsilon = \frac{\dot{V}_0}{2W_\varepsilon} \;\leq\; e^{-k_x t}\big(A\, W_\varepsilon + B\big), \qquad A := 4k_y v_r |x_e(0)|, \quad B := \tfrac{\omega_{\max}+k_\theta}{\sqrt{2}}\,|x_e(0)|.$$

This linear comparison inequality is integrated by the substitution $\Phi(t) := \frac{A}{k_x}\big(1 - e^{-k_x t}\big) \leq \frac{A}{k_x}$:

$$W_\varepsilon(t) \;\leq\; e^{\Phi(t)}\Big[W_\varepsilon(0) + \frac{B}{k_x}\Big] \;\leq\; e^{A/k_x}\Big[W_\varepsilon(0) + \frac{B}{k_x}\Big],$$

because $\int_0^t e^{-k_x s}e^{-\Phi(s)}\,ds \leq \int_0^\infty e^{-k_x s}\,ds = \frac{1}{k_x}$. Letting $\varepsilon \downarrow 0$ yields the time-independent uniform bound

$$W(t) \;\leq\; \bar{W} := e^{A/k_x}\Big[\sqrt{V_0(0)} + \frac{B}{k_x}\Big], \qquad \forall\, t \geq 0.$$

Hence, $|y_e(t)| \le \sqrt{2}\,\bar{W}$ and $|\Theta(t)| \le \sqrt{2k_y}\,\bar{W}$ for all $t \ge 0$. Thus the (y_e, Θ)-subsystem remains bounded during the entire transient in which x_e decays from $|x_e(0)|$ to zero, although it is continuously driven by the coupling input $g(z)x_e$ in (14).

Step 2 (convergence of (y_e, Θ)): By Step 1, y_e, Θ, and $\omega(z)$ are bounded. Integrating the identity $\dot{V}_0 = -\frac{k_\theta}{k_y}\Theta^2 - x_e\,\omega(z)\,y_e$ over $[0,\infty)$ and using $|x_e\omega(z)y_e| \le |x_e(0)|e^{-k_x t}\big(\omega_{\max} + k_\theta + 4k_y v_r \sup_t |y_e|\big) \in L^1[0,\infty)$, we obtain $\frac{k_\theta}{k_y}\int_0^\infty \Theta^2\,\mathrm{d}t \le V_0(0) + \int_0^\infty |x_e\omega(z)y_e|\,\mathrm{d}t < \infty$, i.e., $\Theta \in L^2[0,\infty)$. Moreover, $\dot{\Theta} = -k_\theta\Theta - \frac{2k_y v_r y_e}{1+\Theta^2}$ is bounded, so Θ is uniformly continuous, and Barbalat's lemma [25] yields $\Theta(t) \to 0$. Furthermore, $\ddot{\Theta}$ is bounded: differentiating $\dot{\Theta}$ involves only y_e, Θ, $\dot{\Theta}$, and $\dot{y}_e$, all bounded, where $\dot{y}_e = -x_e\omega(z) + v_r\frac{2\Theta}{1+\Theta^2}$ is bounded by Step 1 and Assumption 1. Hence, $\dot{\Theta}$ is uniformly continuous, and since $\Theta \to 0$, the standard corollary of Barbalat's lemma gives $\dot{\Theta}(t) \to 0$. Finally, solving (13) for y_e (with $v_r \ge v_{\min} > 0$ by Assumption 2 and v_r constant by Assumption 3),

$$y_e = -\frac{1+\Theta^2}{2k_y v_r}\big(\dot{\Theta} + k_\theta\Theta\big) \;\longrightarrow\; 0,$$

and $\theta_e = 2\arctan\Theta \to 0$.

Step 3 (assembly): By Step 2, $(y_e, \Theta) \to (0,0)$ for every initial condition—i.e., the equilibrium of the (y_e, Θ)-subsystem is globally attractive—and by Step 1 all signals remain bounded for arbitrary initial conditions. Lyapunov stability of the origin follows from the explicit bound $\bar{W}$: as $\|(x_e(0), z(0))\| \to 0$ we have $|x_e(0)| \to 0$; hence, $A, B \to 0$, $e^{A/k_x} \to 1$ and $\bar{W} \to \sqrt{V_0(0)}$, so sufficiently small initial conditions produce uniformly small trajectories. Together with the global exponential stability of x_e and the exact solution (16), the equilibrium $(x_e, y_e, \Theta) = (0,0,0)$ of the closed loop (11)–(13) is globally asymptotically stable. □

Remark 1 (Angular-domain invariance). *By Step 1 of the proof of Theorem 1, $V_0(t) \le \bar{V} := \bar{W}^2$ for all $t \ge 0$, where $\bar{W} = e^{A/k_x}[\sqrt{V_0(0)} + B/k_x]$ is the explicit bound constructed in the proof. Since V_0 is radially unbounded, the sublevel set $\{V_0 \le \bar{V}\}$ is compact, and therefore*

$$|\Theta(t)| \;\le\; \sqrt{2k_y\bar{V}} \;=:\; \bar{\Theta} \;<\; \infty, \qquad \forall\, t \ge 0.$$

Because $\Theta = \tan(\theta_e/2)$ is a smooth bijection from $(-\pi,\pi)$ onto $\mathbb{R}$ with inverse $\theta_e = 2\arctan\Theta \in (-\pi,\pi)$, the uniform bound on $\Theta(t)$ implies $|\theta_e(t)| < \pi$ for all $t \ge 0$: the closed-loop trajectory never reaches the stereographic singularity, and the controller operates globally without unwinding. We emphasise the logic of the argument: the boundedness of V_0 follows from the explicit comparison estimate in Step 1, which is valid even though $\dot{V}_0$ is not sign-definite along the full cascade; the radial unboundedness of V_0 then converts the bound on V_0 into a uniform bound on Θ, and hence into the invariance of the angular domain.

3.3. Time-Scale Separation and Predictable Convergence

Theorem 1 guarantees asymptotic convergence but does not directly quantify the settling time. We now extract an explicit relationship between the controller gains and the convergence rates through a linearised time-scale separation analysis.

Linearizing the closed-loop system (11)–(13) around the origin in the original heading coordinates, and retaining the reference angular velocity ω_r, gives

$$\dot{x}_e = -k_x x_e, \tag{17}$$

$$\dot{y}_e = -\omega_r x_e + v_r\theta_e, \tag{18}$$

$$\dot{\theta}_e = -k_\theta\theta_e - 4k_y v_r y_e. \tag{19}$$

Here the origin is an equilibrium of the closed loop for every constant ω_r, and the term $-\omega_r x_e$ in (18) originates from $\partial\dot{y}_e/\partial x_e = -\omega\big|_{\mathbf{e}=0} = -\omega_r$ by the control law (10), while $\partial\dot{y}_e/\partial\theta_e\big|_{\mathbf{e}=0} = v_r$, $\partial\dot{\theta}_e/\partial y_e\big|_{\mathbf{e}=0} = -4k_y v_r$, and $\partial\dot{\theta}_e/\partial\theta_e\big|_{\mathbf{e}=0} = -k_\theta$. In matrix form, the Jacobian of the linearisation is

$$J = \begin{bmatrix} -k_x & 0 & 0 \\ -\omega_r & 0 & v_r \\ 0 & -4k_y v_r & -k_\theta \end{bmatrix}. \tag{20}$$

Since the first row of J contains only its diagonal entry, J is block-lower-triangular with respect to the partition $\big(x_e \,|\, (y_e, \theta_e)\big)$, with diagonal blocks $-k_x$ and $\left[\begin{smallmatrix} 0 & v_r \\ -4k_y v_r & -k_\theta \end{smallmatrix}\right]$. Consequently,

$$\det(\lambda I - J) \;=\; (\lambda + k_x)\big(\lambda^2 + k_\theta\lambda + 4k_y v_r^2\big), \tag{21}$$

and the reference angular velocity ω_r—which enters J only through the feedforward entry $-\omega_r$ in position $(2,1)$, injecting the exponentially decaying signal x_e into the $\dot{y}_e$ channel without any feedback—does not appear in the characteristic polynomial. The time constants $\tau_x = 1/k_x$ and τ_y in (23) below, as well as the separation ratio κ introduced below, are therefore strictly invariant to the constant reference angular velocity ω_r: the gain-to-performance map in Table 1 holds for any constant ω_r, in particular for $\omega_r \neq 0$, and none of the results in this paper require $\omega_r = 0$. This invariance mirrors the exact feedforward cancellation of ω_r in (10), is consistent with the block-triangular spectral argument used in the recovery analysis of Section 4.2, and is confirmed empirically in Section 5.1, where the predicted time constants are verified to within 1% for a circular reference with $\omega_r = 0.5\,\mathrm{rad/s} \neq 0$.

The second-order factor in (21) governs the coupled (y_e, θ_e) dynamics. Its discriminant is $\Delta = k_\theta^2 - 16k_y v_r^2 = \big(k_\theta - 4v_r\sqrt{k_y}\big)\big(k_\theta + 4v_r\sqrt{k_y}\big)$, so a clear mode separation requires k_θ to be much larger than $4v_r\sqrt{k_y}$; since k_y carries the unit m^{-2}, both sides of the separation condition below have the unit s^{-1}.

Under the time-scale separation condition,

$$k_\theta \gg 4v_r\sqrt{k_y}, \tag{22}$$

with the dimensionless separation ratio $\kappa := k_\theta/(4v_r\sqrt{k_y})$. Any $\kappa > 1$ already guarantees that the two roots $\lambda_{f,s} = \frac{-k_\theta \pm \sqrt{\Delta}}{2}$ are real, distinct, and negative, which is all that the recovery analysis of Section 4.2 requires; throughout this paper we adopt the conservative design rule $\kappa \geq 2.5$, under which $\sqrt{\Delta} = k_\theta\sqrt{1-\kappa^{-2}} \geq 0.91\,k_\theta$ and the two modes are clearly separated; a standard singular perturbation analysis [26] shows that the two eigenvalues are well separated:

$$\lambda_f \approx -k_\theta, \qquad \lambda_s \approx -\frac{4k_y v_r^2}{k_\theta}.$$

The fast mode corresponds to the rapid decay of θ_e at rate k_θ, while the slow mode governs the asymptotic decay of y_e with time constant

$$\tau_y \approx \frac{k_\theta}{4k_y v_r^2}. \tag{23}$$

Thus, after an initial fast transient, the lateral error evolves essentially as $|y_e(t)| \propto e^{-t/\tau_y}$. For a slowly varying reference speed $v_r(t)$, (23) admits the frozen-parameter interpretation $\tau_y(t) = k_\theta/(4k_y v_r^2(t))$, which is the form used in the time-varying simulations of Section 5.2.

The longitudinal error is completely decoupled and satisfies $|x_e(t)| = |x_e(0)|e^{-k_x t}$, corresponding to the time constant $\tau_x = 1/k_x$. Consequently, both settling times are explicitly prescribed by the designer through the choice of k_x, k_y and k_θ.

Table 1. From desired settling times to controller gains (constant $v_r > 0$).

Error Channel	Time Const.	Gain Formula	Example ($v_r = 1.0$ m/s)
Longitudinal x_e	$\tau_x = 1/k_x$	$k_x = 1/\tau_x$	$\tau_x = 0.5$ s $\Rightarrow k_x = 2.0$
Lateral y_e (slow)	$\tau_y \approx \frac{k_\theta}{4k_y v_r^2}$	$k_\theta = 4k_y v_r^2 \tau_y$	$\tau_y = 5.0$ s, $k_y = 1 \Rightarrow k_\theta = 20.0$
Heading θ_e (fast transient)	$\tau_\theta \approx 1/k_\theta$	$k_\theta \gg 4v_r\sqrt{k_y}$ ($\kappa \geq 2.5$)	$4v_r\sqrt{k_y} = 4.0$ ($\kappa = 5$), $k_\theta = 20$ ($\tau_\theta \approx 0.05$ s) satisfies separation

3.4. Gain Tuning for Prescribed Performance

Equations $\tau_x = 1/k_x$ and (23) provide a direct map from desired settling times to controller gains. Table 1 summarises this mapping and gives a numerical example that satisfies the separation condition.

Unlike x_e, whose exponential decay is exact, and y_e, which follows the single slow mode after the fast transient, θ_e exhibits a two-phase response: it first approaches the slow manifold $\theta_e \approx -(4k_y v_r/k_\theta)\, y_e$ at the fast-eigenvalue rate $|\lambda_f| = \frac{k_\theta}{2}\left(1 + \sqrt{1 - \kappa^{-2}}\right)$, and then decays along that manifold at the slow rate $1/\tau_y$. We therefore define the heading transient constant $\tau_\theta := 1/|\lambda_f|$, which under $\kappa \geq 2.5$ satisfies $1/k_\theta \leq \tau_\theta \leq 1.05/k_\theta$, whence $\tau_\theta \approx 1/k_\theta$ within 5%. The 5% settling time of θ_e is nevertheless governed by the slow phase and occurs slightly earlier than that of y_e, since the slaving ratio $4k_y v_r/k_\theta$ scales the lateral error down (e.g., 6.34 s vs. 7.66 s in Table 2); τ_θ thus prescribes the initial heading transient, while the overall heading settling remains tied to τ_y.

The tuning procedure is systematic and requires no trial-and-error:

1. Select k_x from the desired longitudinal settling time τ_x via $k_x = 1/\tau_x$.
2. Choose k_y (typically $k_y = 1$) and the desired lateral settling time τ_y; compute $k_\theta = 4k_y v_r^2 \tau_y$.
3. Verify the separation ratio $\kappa = k_\theta/(4v_r\sqrt{k_y}) \geq 2.5$; if necessary, increase k_θ while proportionally adjusting k_y so that τ_y remains unchanged. If the required k_θ becomes too large, a slightly larger τ_y can be accepted.

Table 2. Performance comparison for the circular trajectory with large initial error (Case B).

Controller	Error	Settling Time (s)	Max $\lvert e \rvert$	ISE	End-of-Run Residual
Proposed	x_e	1.27	2.000	1.6555	$\approx 4.2 \times 10^{-9}$
	y_e	7.66	1.375	3.0700	—
	θ_e	6.34	1.571	1.3764	—
Kanayama	x_e	2.59	2.000	1.2383	$\approx -3.0 \times 10^{-3}$
	y_e	19.62	1.112	3.8038	—
	θ_e	6.65	1.571	0.9105	—
Bai et al.	x_e	1.22	2.000	1.3328	$\approx 4.7 \times 10^{-6}$
	y_e	4.64	0.907	1.0153	—
	θ_e	4.31	1.571	1.3876	—

Equivalently, the tuning can be performed entirely in the time-constant domain: prescribe the three desired constants $(\tau_x, \tau_y, \tau_\theta)$ and set $k_x = 1/\tau_x$, $k_\theta = 1/\tau_\theta$, and $k_y = 1/(4v_r^2\, \tau_y\, \tau_\theta)$. In these variables the separation ratio takes the closed form $\kappa = \frac{1}{2}\sqrt{\tau_y/\tau_\theta}$, so the design rule $\kappa \geq 2.5$ reduces to the single requirement $\tau_y \geq 25\, \tau_\theta$: the prescribed lateral time constant must exceed the prescribed heading transient by a factor of 25. For the gains of Section 5 ($k_\theta = 32$, $k_y = 4$, $v_r = 1$ m/s), this gives $\tau_\theta \approx 1/32$ s, $\tau_y = 2$ s, $k_y = 4$, and $\kappa = 4$, reproducing Table 1 and the parameters used in the simulations.

Remark 2. *Since the origin is an equilibrium of the closed loop for every constant ω_r and the gain-to-performance map in Table 1 is strictly invariant to ω_r (Section 3.3), all results in Sections 3 and 4 apply verbatim within each constant segment of a piecewise-constant reference (v_r, ω_r)—i.e., to paths composed of straight segments ($\omega_r = 0$) and circular arcs ($\omega_r = \text{const}$), the Dubins-type paths underlying many navigation and parking maneuvers. Within each segment the prescribed time constants τ_x, τ_y hold as designed. Across segment boundaries the error $\mathbf{e}$ is continuous (it depends on the poses $\mathbf{q}$ and $\mathbf{q}_r$ only, and $\mathbf{q}_r$ is continuous for piecewise-continuous (v_r, ω_r)), so each new segment starts from the error state reached at the switch and converges afresh at the prescribed rates.*

Because the longitudinal channel is exactly decoupled, tuning k_x has no effect on the lateral dynamics, and vice versa. This predictable performance baseline is the foundation on which the obstacle-aware extension of Section 4 is built: even in the presence of obstacles, the nominal convergence rates dictate how quickly the robot recovers precise tracking after an avoidance maneuver.

4. Structure-Preserving Obstacle Avoidance with Predictable Performance

4.1. Control Law and Perturbed Cascade Model

We now extend the nominal predictable-performance controller to handle static obstacles. The core idea is to superimpose an APF-based correction in a structure-preserving manner, maintaining exact longitudinal decoupling and the cascade form. Recall that the nominal controller (10) uses the term $y_e\omega$ in v to cancel the coupling in $\dot{x}_e$. If an angular velocity correction $\Delta\omega_{\text{obs}}$ is added without updating this cancellation term, the longitudinal dynamics become $\dot{x}_e = -k_x x_e + y_e \Delta\omega_{\text{obs}}$, re-introducing coupling. To preserve the exact decoupling, we must use the actual angular velocity $\omega = \omega_{\text{trk}} + \Delta\omega_{\text{obs}}$ in $y_e\omega$. This yields the obstacle-aware control law:

$$\begin{aligned} v &= y_e\omega + v_r \frac{1-\Theta^2}{1+\Theta^2} + k_x x_e + \Delta v_{\text{obs}}, \\ \omega &= \omega_r + \frac{2k_\theta \Theta}{1+\Theta^2} + \frac{4k_y v_r y_e}{(1+\Theta^2)^2} + \Delta\omega_{\text{obs}}, \end{aligned} \tag{24}$$

where $\Theta = \tan(\theta_e/2)$ and Δv_{obs} and $\Delta\omega_{\text{obs}}$ are APF-based corrections defined below.

For N static obstacles at $\mathbf{o}_i = [x_{oi}, y_{oi}]^\top$, $i = 1, \ldots, N$, let $d_i = \|\mathbf{p} - \mathbf{o}_i\|$ and ϕ_i be the relative bearing in the robot body frame (Section 2.3). Using the repulsive potential (8), the velocity corrections are

$$\begin{aligned} \Delta v_{\text{obs}} &= -\alpha \sum_{d_i < d_0} \Big(\frac{1}{d_i} - \frac{1}{d_0}\Big) \frac{\cos\phi_i}{d_i^2}, \\ \Delta\omega_{\text{obs}} &= -\beta \sum_{d_i < d_0} \Big(\frac{1}{d_i} - \frac{1}{d_0}\Big) \frac{\sin\phi_i}{d_i^2}, \end{aligned} \tag{25}$$

with gains $\alpha, \beta > 0$ and influence radius $d_0 > 0$. To respect actuator limits, the corrections are saturated to $[\Delta v_{\min}, \Delta v_{\max}]$ and $[\Delta\omega_{\min}, \Delta\omega_{\max}]$, ensuring boundedness:

$$|u_1(t)| \le \bar{u}_1, \quad |u_2(t)| \le \bar{u}_2, \qquad u_1 := -\Delta v_{\text{obs}},\ u_2 := \Delta\omega_{\text{obs}}. \tag{26}$$

In addition to the saturation above, the angular correction is gated with respect to the heading error so as to respect the angular-domain condition of Assumption 4: the angular correction is applied only while the heading error remains moderate and is set to zero otherwise,

$$\Delta\omega_{\text{obs}} \ \leftarrow\ \chi(\theta_e)\,\Delta\omega_{\text{obs}}, \qquad \chi(\theta_e) = \begin{cases} 1, & |\theta_e| \le \theta_{\text{gate}}, \\ 0, & |\theta_e| > \theta_{\text{gate}}, \end{cases} \tag{27}$$

with a design threshold $\theta_{\text{gate}} \in (0, \pi)$ (e.g., $\theta_{\text{gate}} = 1.2$ rad in Section 5). The gate suppresses the angular correction precisely in the regime where it could drive θ_e toward the stereographic singularity. Since gating can only reduce the correction magnitude, the gated correction still satisfies the bound $|u_2| \le \bar{u}_2$ in (26), and the boundedness analysis of Theorem 2 applies unchanged. The longitudinal correction Δv_{obs} is not gated, because it does not affect the angular-domain condition.

Substituting (24) into (7) and using the actual ω in the $y_e\omega$ term, the closed-loop system becomes

$$\begin{aligned} \dot{x}_e &= -k_x x_e + u_1, \\ \dot{z} &= f(z) + g(z)x_e + p(z)u_2 + q(x_e)u_2, \end{aligned} \tag{28}$$

where $z = [y_e, \Theta]^\top$, $f(z)$ and $g(z)$ are as in (14), and

$$p(z) = \begin{bmatrix} 0 \\ -\frac{1+\Theta^2}{2} \end{bmatrix}, \qquad q(x_e) = \begin{bmatrix} -x_e \\ 0 \end{bmatrix}.$$

When $u_1 \equiv u_2 \equiv 0$, system (28) exactly recovers the nominal cascade, which is globally asymptotically stable by Theorem 1.

The overall structure of the proposed control scheme, including the gated and saturated APF corrections and the structure-preserving feedback of the actual angular velocity ω into the longitudinal cancellation term $y_e\omega$, is illustrated in Figure 2. Moreover, the reading order of the diagram mirrors the order in which the controller is constructed in this paper. The upper row assembles the nominal tracking layer of Sections 2 and 3: the error-computation block evaluates the tracking errors and the stereographic coordinate (Equations (3) and (5)); the tracking-law block implements the three-stage design of Section 3—exact longitudinal decoupling, cascade stability (Theorem 1), and time-scale separation; and the superposition–saturation block enforces the actuator bounds under which the boundedness analysis of Section 4.2 is conducted. The lower row realises the avoidance layer of this section: the APF block computes the corrections (25) and (26), subject to the heading-error gate (27), from the robot position and the obstacle map. By design, the two layers are coupled at exactly two points: the corrections are added to the nominal commands only inside the superposition block, and the resulting actual angular velocity is routed back along the thick path into the $y_e\omega$ cancellation term—the single structural modification that keeps the longitudinal dynamics exactly of the form $\dot{x}_e = -k_x x_e + u_1$ and allows the Lyapunov analysis of Section 4.2 to reuse, rather than redo, the nominal cascade argument of Theorem 1. Whenever the corrections vanish ($u_1 = u_2 = 0$), the lower row becomes inactive and the diagram collapses to the nominal loop, so that each stage of the development reduces exactly to the preceding one.

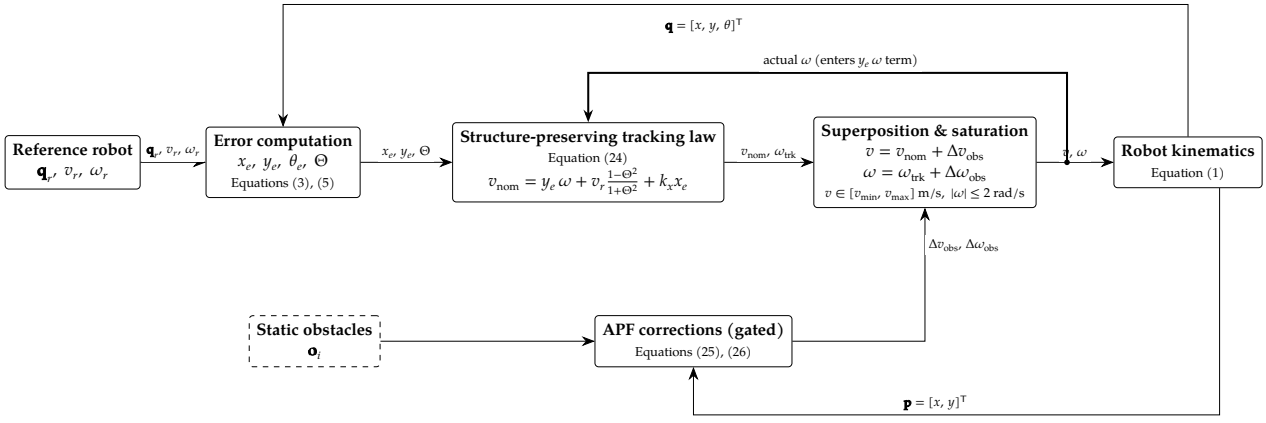


Figure 2. Block diagram of the proposed structure-preserving control scheme.

4.2. Boundedness and Recovery Analysis

Although the nominal z-subsystem is globally asymptotically stable, it does not show input-to-state stability (ISS) with respect to the coupling input: for a constant negative coupling signal $x_e \equiv -\delta < 0$, the interconnection term in (12) contains the anti-damping component $4k_y v_r \delta\, y_e^2$, under which y_e grows without bound. Consequently, we can establish the practically essential property of bounded-input bounded-state (BIBS) stability [27], together with the guarantee that tracking precision eventually recovers at the nominal rates once the obstacle is cleared. We remark that boundedness of the corrections u_1, u_2 alone would not suffice to keep Θ bounded, since u_2 enters the Θ-dynamics through the factor $(1+\Theta^2)/2$ in (28); the analysis below is therefore conducted under the angular-domain condition of Assumption 4, which is the standing design requirement for the obstacle-aware case and is verified a posteriori in Section 5.

Theorem 2 (BIBS stability and asymptotic recovery)**.** *Consider the perturbed cascade* (28) *with bounded inputs* $|u_1(t)| \le \bar{u}_1$, $|u_2(t)| \le \bar{u}_2$. *Let Assumptions 1–5 hold. Throughout the statement,* t_{out} *denotes the time at which the robot exits the obstacle influence zone (finite by Assumption 5), and the avoidance maneuver is assumed to preserve the angular domain, i.e.,* $|\theta_e(t)| < \pi$ *on the avoidance interval* $[0, t_{\text{out}}]$*; equivalently, since* $\theta_e \mapsto \tan(\theta_e/2)$ *is continuous and* $[0, t_{\text{out}}]$ *is compact, there exists a finite constant* $\bar{\Theta}$ *such that* $|\Theta(t)| \le \bar{\Theta}$ *for all* $t \in [0, t_{\text{out}}]$ *(Assumption 4). Then:*

(i) Uniform boundedness: All closed-loop states remain uniformly bounded for all $t \ge 0$. *In particular,*

$$|x_e(t)| \le e^{-k_x t}|x_e(0)| + \frac{\bar{u}_1}{k_x} \le |x_e(0)| + \frac{\bar{u}_1}{k_x}, \tag{29}$$

$$\|z(t)\| \le \Gamma\big(\|z(0)\|, \bar{x}_e, \bar{u}_2\big), \tag{30}$$

where Γ *is a computable function, whose explicit expression is constructed in the proof below; in addition to its displayed arguments,* Γ *also depends on the a priori angular bound* $\bar{\Theta}$*, on the avoidance duration* t_{out}*, and on the controller and reference parameters and* $\bar{x}_e = |x_e(0)| + \bar{u}_1/k_x$.

(ii) Eventual predictable recovery: If the robot exits the obstacle influence zone at $t = t_{\text{out}}$ *(so that* $u_1 \equiv u_2 \equiv 0$ *for all* $t \ge t_{\text{out}}$*), then*

$$\lim_{t\to\infty}(x_e, y_e, \theta_e) = (0, 0, 0),$$

and the convergence is exponential after a finite transient, provided that the longitudinal mode is not slower than the lateral slow mode, i.e., $k_x \ge 1/\tau_y$ *(equivalently,* $k_x k_\theta \ge 4k_y v_r^2$*). In particular, the longitudinal error satisfies* $|x_e(t)| = |x_e(t_{\text{out}})|e^{-(t-t_{\text{out}})/\tau_x}$*, and there exist constants* $T \ge t_{\text{out}}$ *and* $C_0 > 0$ *such that*

$$|y_e(t)| \le C_0 e^{-(t-T)/\tau_y} \qquad \text{for all } t \ge T,$$

with $\tau_x = 1/k_x$ *and* $\tau_y = k_\theta/(4k_y v_r^2)$.

Proof. (i) Longitudinal bound: Equation (29) follows directly from the explicit solution of $\dot{x}_e = -k_x x_e + u_1$.

(ii) Boundedness of z: Consider the Lyapunov function $V_0(z) = \frac{1}{2}y_e^2 + \frac{1}{2k_y}\Theta^2$. Its derivative along (28) is

$$\dot{V}_0 = -\frac{k_\theta}{k_y}\Theta^2 \;-\; x_e\,\omega_{\text{trk}}(z)\,y_e \;-\; x_e u_2 y_e \;-\; \frac{\Theta(1+\Theta^2)}{2k_y}u_2. \tag{31}$$

The correction terms are bounded globally, without any a priori boundedness assumption on the state. Using $\left|\frac{2\Theta}{1+\Theta^2}\right| \le 1$, $(1+\Theta^2)^{-2} \le 1$, $|y_e| \le \sqrt{2V_0}$, and $|x_e(t)| \le \bar{x}_e$ from (29), the angular velocity command obeys

$$|\omega_{\text{trk}}(z)| \le \omega_{\max} + k_\theta + 4k_y v_r |y_e|,$$

with $\omega_{\max}$ from Assumption 1, whence the second and third terms in (31) satisfy

$$|x_e\,\omega_{\mathrm{trk}}(z)\,y_e| \le \sqrt{2}\,\bar{x}_e(\omega_{\max}+k_\theta)\,V_0^{1/2} + 8k_y v_r \bar{x}_e\,V_0,$$
$$|x_e u_2 y_e| \le \sqrt{2}\,\bar{x}_e \bar{u}_2\,V_0^{1/2}.$$

On the avoidance interval $[0, t_{\mathrm{out}}]$, the angular-domain condition provides the a priori bound $|\Theta(t)| \le \bar{\Theta}$, so that the last term in (31) is an additive constant,

$$\frac{|\Theta|(1+\Theta^2)}{2k_y}\bar{u}_2 \;\le\; \frac{\bar{u}_2\,\bar{\Theta}(1+\bar{\Theta}^2)}{2k_y} \;=:\; c.$$

Collecting the estimates and discarding the negative term $-\frac{k_\theta}{k_y}\Theta^2$ yields

$$\dot{V}_0 \;\le\; aV_0 + bV_0^{1/2} + c, \qquad a := 8k_y v_r \bar{x}_e, \quad b := \sqrt{2}\,\bar{x}_e\,(\omega_{\max}+k_\theta+\bar{u}_2).$$

By Young's inequality $bV_0^{1/2} \le \frac{b^2}{2k_x} + \frac{k_x}{2}V_0$ and the Grönwall comparison lemma,

$$\dot{V}_0 \le \alpha_c V_0 + \beta, \qquad \alpha_c := a + \frac{k_x}{2}, \quad \beta := c + \frac{b^2}{2k_x},$$

$$V_0(t) \;\le\; e^{\alpha_c t}[V_0(0)+\beta t] \;\le\; e^{\alpha_c t_{\mathrm{out}}}[V_0(0)+\beta\,t_{\mathrm{out}}] \;=:\; \Gamma_V, \qquad \forall\, t \in [0, t_{\mathrm{out}}],$$

where the last inequality uses $\int_0^t e^{\alpha_c(t-s)}\,\mathrm{d}s \le t\,e^{\alpha_c t}$. For $t \ge t_{\mathrm{out}}$ the inputs vanish and $x_e(t) = x_e(t_{\mathrm{out}})e^{-k_x(t-t_{\mathrm{out}})}$; applying the uniform bound of Step 1 in the proof of Theorem 1, initialised at t_{out}, gives

$$V_0(t) \;\le\; e^{\frac{8k_y v_r \bar{x}_e}{k_x}}\Big[\Gamma_V^{1/2} + \frac{(\omega_{\max}+k_\theta)\bar{x}_e}{\sqrt{2}\,k_x}\Big]^2, \qquad \forall\, t \ge t_{\mathrm{out}}.$$

Combining both intervals and using $\|z\|^2 = y_e^2 + \Theta^2 \le 2(1+k_y)V_0$ establishes (30) with the explicit function

$$\Gamma \;=\; \sqrt{2(1+k_y)}\,\max\Big\{\,\Gamma_V^{1/2},\; e^{\frac{4k_y v_r \bar{x}_e}{k_x}}\Big[\Gamma_V^{1/2} + \frac{(\omega_{\max}+k_\theta)\bar{x}_e}{\sqrt{2}\,k_x}\Big]\Big\},$$

which depends on $\|z(0)\|$ through $V_0(0) \le \frac{\max(1,1/k_y)}{2}\|z(0)\|^2$, on $\bar{x}_e$ (hence on $|x_e(0)|$ and $\bar{u}_1$), on $\bar{u}_2$ through b and c, on the a priori bound $\bar{\Theta}$, on the avoidance duration t_{out}, and on the gains and reference bounds $(k_x, k_y, k_\theta, v_r, \omega_{\max})$. Finally, $|\theta_e(t)| < \pi$ for all $t \ge 0$: on $[0, t_{\mathrm{out}}]$ by the angular-domain condition, and for $t \ge t_{\mathrm{out}}$ by Remark 1 applied to the nominal cascade.

(iii) Recovery: For $t \ge t_{\mathrm{out}}$, $u_1 \equiv u_2 \equiv 0$, and (28) reduces to the nominal cascade. Write $\xi = [x_e, y_e, \Theta]^{\mathsf{T}}$ and $\dot{\xi} = F(\xi)$ for the nominal vector field, which is smooth on $\mathbb{R}^3$ since the denominators $1+\Theta^2$ never vanish. The Jacobian $J = DF(0)$ is block-lower-triangular, with diagonal blocks $-k_x$ and $\begin{bmatrix} 0 & 2v_r \\ -2k_y v_r & -k_\theta \end{bmatrix}$; hence, its eigenvalues are $-k_x$ together with the roots $\lambda_{f,s} = \frac{-k_\theta \pm \sqrt{k_\theta^2 - 16k_y v_r^2}}{2}$ of $\lambda^2 + k_\theta\lambda + 4k_y v_r^2 = 0$, independently of ω_r. Decomposing $F(\xi) = J\xi + h(\xi)$, smoothness gives $h(0) = 0$, $Dh(0) = 0$, and there exist $r > 0$ and $c_h > 0$ such that $\|h(\xi)\| \le c_h\|\xi\|^2$ for $\|\xi\| \le r$. Under (22) with $\kappa \ge 2.5$ (indeed, any $\kappa > 1$ suffices), the three eigenvalues are real, negative, and distinct, and

$$|\lambda_s| = \frac{k_\theta}{2}\Big(1 - \sqrt{1-\kappa^{-2}}\Big) > \frac{k_\theta}{4\kappa^2} = \frac{1}{\tau_y}, \qquad |\lambda_f| \ge \frac{k_\theta}{2} > \frac{1}{\tau_y},$$

where the first inequality uses $\sqrt{1-x} < 1 - \frac{x}{2}$ for $x \in (0,1)$ together with $k_\theta/(4\kappa^2) = 4k_y v_r^2/k_\theta = 1/\tau_y$, and the second holds because (22) with $\kappa > 1$ gives $k_\theta^2 > 16k_y v_r^2 > 8k_y v_r^2$.

Since $k_x \geq 1/\tau_y$ by assumption, $\lambda_* := \min\{k_x, |\lambda_f|, |\lambda_s|\} \geq 1/\tau_y$; since J is diagonalisable, there exists $C \geq 1$ with $\|e^{J\tau}\| \leq Ce^{-\lambda_*\tau}$ for all $\tau \geq 0$. By Theorem 1 applied with initial time t_{out}, $\xi(t) \to 0$; hence, for any $r' \leq \min\{r, \lambda_*/(4c_hC^2)\}$ there exists $T_1 \geq t_{\text{out}}$ with $\|\xi(T_1)\| \leq r'$. For $t \geq T_1$, variation in constants gives $\xi(t) = e^{J(t-T_1)}\xi(T_1) + \int_{T_1}^{t} e^{J(t-s)}h(\xi(s))\,\mathrm{d}s$, so that, with $\psi(t) := e^{\lambda_*(t-T_1)}\|\xi(t)\|$,

$$\psi(t) \;\leq\; C\|\xi(T_1)\| + Cc_h \int_{T_1}^{t} \psi(s)\,\|\xi(s)\|\,\mathrm{d}s.$$

We claim $\psi(t) \leq K := 2C\|\xi(T_1)\|$ for all $t \geq T_1$. Let $\mathcal{T} := \sup\{\tau \geq T_1 : \psi(s) \leq K \text{ on } [T_1, \tau]\}$. On $[T_1, \mathcal{T})$, using $\|\xi(s)\| = e^{-\lambda_*(s-T_1)}\psi(s) \leq Ke^{-\lambda_*(s-T_1)}$,

$$\psi(t) \;\leq\; C\|\xi(T_1)\| + Cc_hK^2 \int_{T_1}^{t} e^{-\lambda_*(s-T_1)}\,\mathrm{d}s \;\leq\; C\|\xi(T_1)\| + \frac{Cc_hK^2}{\lambda_*} \;\leq\; 2C\|\xi(T_1)\| \;=\; K,$$

where the last inequality is precisely the condition $\|\xi(T_1)\| \leq \lambda_*/(4c_hC^2)$. By continuity of ψ, $\mathcal{T} = \infty$. Consequently,

$$|y_e(t)| \;\leq\; \|\xi(t)\| \;\leq\; K\,e^{-\lambda_*(t-T_1)} \;\leq\; C_0\,e^{-(t-T_1)/\tau_y}, \qquad t \geq T_1,$$

with $C_0 := 2C\|\xi(T_1)\|$ and $T := T_1 \geq t_{\text{out}}$, which is the claimed exponential recovery at the prescribed lateral time constant. The claim $\lim_{t\to\infty}(x_e, y_e, \theta_e) = (0, 0, 0)$ follows from $x_e(t) = x_e(t_{\text{out}})e^{-(t-t_{\text{out}})/\tau_x}$, $(y_e, \Theta) \to 0$, and $\theta_e = 2\arctan\Theta$. □

Theorem 2 provides a boundedness and recovery guarantee rather than a formal safety certificate: tracking errors remain uniformly bounded during the avoidance maneuver, and once the obstacle is cleared, precision tracking resumes with the recovery rate dictated by the prescribed nominal time constants τ_x and τ_y. Forward invariance of the collision-free set is not claimed; collision avoidance is ensured at the design level, through the selection of the APF parameters and of d_0 under Assumption 5 (in particular the condition $d_i(t) \geq d_{\min}$), and is verified a posteriori in Section 5. Enforcing forward invariance via a control barrier function certificate is a complementary approach that could be combined with the structure-preserving design; this extension is left for future work.

4.3. Quantitative Performance Prediction

While Theorem 2 guarantees boundedness and recovery, it does not provide explicit bounds on the tracking errors during the avoidance maneuver. We now derive such bounds, which enable the designer to assess mission-specific error tolerances without exhaustive simulation.

Corollary 1 (Conservative error bounds during avoidance)**.** *Under the conditions of Theorem 2, the peak tracking deviations satisfy*

$$\|x_e\|_\infty \leq |x_e(0)| + \frac{\alpha}{k_x}\,\Phi(d_0), \tag{32}$$

$$\|y_e\|_\infty \leq \rho_1\big(|y_e(0)|, |\theta_e(0)|\big) + \rho_2(\alpha, \beta, d_0), \tag{33}$$

where $\Phi(d_0)$ is a conservative but computable function that decreases monotonically with d_0, and $\rho_2(\alpha, \beta, d_0)$ is a conservative but computable function that increases monotonically with α, β and decreases monotonically with d_0.

Proof. From the definition of Δv_{obs} in (25) and the saturation bounds (26), we have $\bar{u}_1 \leq \alpha \sum_{d_i < d_0} d_i^{-3}$. During avoidance, the minimum obstacle distance is lower-bounded by a positive constant $d_{\min} > 0$ (Assumption 5). Hence,

$$\bar{u}_1 \leq \alpha N d_{\min}^{-3} =: \alpha\Phi(d_0), \qquad \bar{u}_2 \leq \beta\Phi(d_0),$$

where $\Phi(d_0)$ decreases with d_0 because a larger influence radius leads to earlier, gentler avoidance and a larger $d_{\min}$. Substituting into (29) yields (32).

For the lateral bound, we make the comparison analysis of the proof of Theorem 2(ii) explicit. Substituting $\bar{u}_1 \le \alpha\Phi(d_0)$ and $\bar{u}_2 \le \beta\Phi(d_0)$ into the constants defined there, the bound on the avoidance interval $[0, t_{\text{out}}]$ reads

$$V_0(t) \;\le\; \Gamma_V \;=\; e^{\alpha_c t_{\text{out}}}[V_0(0) + \beta\, t_{\text{out}}],$$

$$\alpha_c = 8k_y v_r \bar{x}_e + \frac{k_x}{2}, \qquad \beta = \frac{\bar{u}_2\,\bar{\Theta}(1+\bar{\Theta}^2)}{2k_y} + \frac{\bar{x}_e^2\,(\omega_{\max} + k_\theta + \bar{u}_2)^2}{k_x}, \qquad \bar{x}_e = |x_e(0)| + \frac{\bar{u}_1}{k_x}.$$

Since $\|y_e\| \le \sqrt{2V_0}$, we have $\|y_e\|_\infty \le \sqrt{2\Gamma_V}$. Writing $\sqrt{2\Gamma_V} = \rho_1 + \rho_2$, where $\rho_1 := \sqrt{2\Gamma_V}\big|_{\bar{u}_1=\bar{u}_2=0}$ depends only on the initial conditions and the nominal parameters (the nominal transient, evaluated with the avoidance duration t_{out}) and $\rho_2 := \sqrt{2\Gamma_V} - \rho_1 \ge 0$ collects the APF-induced contribution, yields exactly the form (33). Because α_c and β are nondecreasing in $\bar{u}_1$ and $\bar{u}_2$, the computable bound Γ_V—and hence ρ_2—is nondecreasing in α, β and, through the decrease in $\Phi(d_0)$ with d_0, nonincreasing in d_0; in particular, $\rho_2(\alpha, \beta, d_0) = O\big((\alpha+\beta)\Phi(d_0)\big)$ for weak corrections. For completeness, ρ_2 also depends on the a priori angular bound $\bar{\Theta}$ entering through c, and on the avoidance duration t_{out}. □

Corollary 1 is the key tool for predictable performance in the obstacle-aware setting. Although the bounds are conservative due to successive inequality relaxations, they faithfully capture the essential monotonic relationships: increasing α, β strengthens the avoidance response at the cost of larger tracking deviations, while increasing d_0 softens the maneuver and reduces deviations. These relationships allow the designer to trade off safety margins against tracking accuracy without relying on extensive simulations.

Remark 3 (Design considerations)**.** *The monotone dependencies in* (32) *and* (33) *provide qualitative guidance for parameter selection. In practice, one first tunes the tracking gains k_x, k_y, k_θ using Table 1 to set the nominal recovery time τ_y. The influence radius d_0 is then chosen based on the required safe distance, and α, β are adjusted to balance avoidance strength against acceptable tracking deviation. More specifically, d_0 is not a free parameter but is constrained by physical and performance requirements: (i) physically, d_0 must exceed the obstacle radius plus the distance traversed by the robot during the reaction and saturation transient of the avoidance maneuver, with a suitable margin, and must remain within the sensor range; (ii) performance-wise, by Corollary 1, enlarging d_0 reduces the worst-case deviation ρ_2 (earlier and gentler steering) at the price of a longer detour from the reference path. In practice, d_0 is set to the smallest physically admissible value, and α, β are then tuned until the deviations predicted by* (32) *and* (33) *meet the mission tolerance. The decoupled longitudinal channel ($\dot{x}_e = -k_x x_e - \Delta v_{\text{obs}}$) ensures that k_x can be tuned independently to control longitudinal recovery.*

5. Numerical Simulation and Validation

To validate the theoretical results established in previous sections and to evaluate the practical effectiveness of the proposed framework, two scenarios are considered. The kinematic model (1) is used throughout, and the control inputs are saturated to represent the velocity bounds of the inner-loop velocity controller: $v \in [0.1, 1.5]$ m/s and $\omega \in [-2.0, 2.0]$ rad/s in the circular scenario of Section 5.1, and $v \in [0.1, 1.7]$ m/s and $\omega \in [-2.0, 2.0]$ rad/s in the figure-eight scenario of Section 5.2. In both scenarios the bound exceeds the corresponding peak reference speed with margin, and all compared controllers share the same actuator set within each scenario.

5.1. Circular Trajectory: Verification of Nominal Predictable Performance

The reference trajectory is a circle of radius $R = 2.0$ m with constant angular speed $\Omega = 0.5$ rad/s:

$$x_r(t) = R\cos(\Omega t), \quad y_r(t) = R\sin(\Omega t), \quad \theta_r(t) = \Omega t + \frac{\pi}{2},$$

yielding constant reference velocities $v_r = 1.0$ m/s and $\omega_r = 0.5$ rad/s. Since v_r and ω_r are constant, this scenario satisfies Assumptions 1–3 exactly, and it is run in two complementary configurations. Case A employs small initial errors, $x_e(0) = y_e(0) = 0.02$ m and $\theta_e(0) = 0.02$ rad, which keep the closed loop in the linear regime and away from input saturation, so that the time constants predicted in Section 3.3 can be verified quantitatively. Case B employs the large initial pose $\mathbf{q}(0) = [0,\ 0,\ 0]^{\mathsf{T}}$, which by (3) corresponds to $x_e(0) = 2$ m, $y_e(0) = 0$ and $\theta_e(0) = \pi/2$ rad; this configuration exercises the input saturation and serves for the comparison of the three controllers.

Three controllers are compared:

1. Proposed nominal controller: The control law (10) with gains $k_x = 8.0$, $k_y = 4.0$, and $k_\theta = 32.0$. These gains follow the tuning guidelines of Section 3 (Table 1) and yield the time constants $\tau_x = 1/k_x = 0.125$ s and $\tau_y = k_\theta/(4k_y v_r^2) = 2.0$ s, while satisfying the separation condition (22) with ratio $\kappa = k_\theta/(4v_r\sqrt{k_y}) = 4 \geq 2.5$.
2. Kanayama controller [6]: The standard form

$$v = v_r\cos\theta_e + k_x x_e, \qquad \omega = \omega_r + k_\theta \sin\theta_e + k_y v_r y_e,$$

with the same gain values $k_x = 8.0$, $k_y = 4.0$, $k_\theta = 32.0$ for a fair comparison.
3. Bai et al. controller [28]: The self-tuning law with an online steepest-descent mechanism. Following the original reference, the initial gains are $k_x = 8.0$, $k_y = 1$, and $k_\theta = 0.4$, learning rates are $\eta_x = \eta_y = \eta_\theta = 0.1$, and $\alpha = \beta = 1$.

Throughout this subsection, the 5% settling time of an error channel is the first time instant after which the error remains within ± 0.05 (in m or rad) at all later times, and the integral squared error is ISE $= \int_0^T e^2\,\mathrm{d}t$ with $T = 20$ s.

Case A (linear regime): None of the three controllers saturates, and the closed loop operates in the regime where the analysis of Section 3.3 applies; the results are shown in Figure 3. The longitudinal error follows (16): regression of $\ln|x_e|$ over $t \in [0.2, 1.5]$ s yields $\hat{\tau}_x = 0.124$ s ($R^2 = 0.99996$), within 1% of the design value $\tau_x = 0.125$ s. For the lateral channel, the heading error decays at the fast rate $\lambda_f \approx -31.5$ s^{-1} within about 0.2 s and is then slaved to the slow lateral mode at the predicted ratio $\theta_e \approx -0.5\,y_e$, observed as a steady-state ratio of -0.50. Regression of $\ln|y_e|$ over $t \in [0.5, 7]$ s yields $\hat{\tau}_y = 2.013$ s ($R^2 = 0.99992$), within 1% of $\tau_y = 2.0$ s and consistent with the slow eigenvalue $\lambda_s = -0.508$ s^{-1} ($1/|\lambda_s| = 1.97$ s); the residual deviation reflects the second-order terms neglected in the linearisation. The tuning procedure of Table 1 thus translates desired settling times into gains without trial and error. We emphasise that this quantitative verification is obtained for a reference moving with $\omega_r = 0.5$ rad/s $\neq 0$: consistent with the spectral invariance established in Section 3.3, the predicted time constants τ_x and τ_y remain valid under a nonzero constant reference angular velocity, and none of the results in this paper rely on $\omega_r = 0$.

Case B (large error and saturation): The performance metrics are summarised in Table 2, and the time histories are depicted in Figure 4. The key difference lies in the end-of-run longitudinal accuracy. The proposed controller drives x_e to $\approx 4.2 \times 10^{-9}$ m (numerical precision), confirming the exact decoupling $\dot{x}_e = -k_x x_e$; Bai et al. leaves 4.7×10^{-6} m. The Kanayama residual is three orders of magnitude larger (-3.0×10^{-3} m) and structural in origin: with $\dot{x}_e = y_e\omega - k_x x_e$, the still-decaying lateral motion ($y_e \approx -4.7 \times 10^{-2}$ m on the slow time-scale $\tau_y^{\mathrm{Kan}} = 8$ s, $\omega \approx 0.5$ rad/s) produces the quasi-static residual $x_e \approx y_e\omega/k_x \approx -2.9 \times 10^{-3}$ m, in agreement with the observed value. The residual vanishes only as $y_e \to 0$; it quantifies the missing $y_e\omega$ cancellation rather than a permanent offset.

For the lateral channel, identical gains map to different performance in the two structures: the linearised slow mode is 2.0 s for the proposed law ($\lambda^2 + k_\theta\lambda + 4k_y v_r^2 = 0$) versus 8.0 s for Kanayama ($\lambda^2 + k_\theta\lambda + k_y v_r^2 = 0$), and the observed settling times (7.66 s vs. 19.62 s) are consistent with these values up to the saturation-induced delay: the large initial heading error necessarily saturates ω (3.1% occupancy; v: 5.3%), which also explains the larger lateral peak (1.375 m). Bai et al. settles fastest laterally (4.64 s) since its adaptive gains are not bound by a prescribed τ_y, but offers no a priori gain-to-performance map or decoupling guarantee, as evidenced by its longitudinal residual.

In all runs $\max_t |\theta_e(t)| = \theta_e(0) = \pi/2 < \pi$, which verifies the angular-domain condition of Assumption 4 a posteriori in the nominal (obstacle-free) case; no unwinding occurs. After the saturation transient, $|x_e|$ resumes the $e^{-k_x t}$ decay (Figure 4), and the lateral error recovers consistently with the prescribed τ_y once the inputs leave saturation.

In summary, the circular results validate the exact longitudinal decoupling to numerical precision, the predictable convergence via the verified time constants, the angular-domain invariance, and bounded recovery under large errors and saturation, while delineating the trade-off between prescribed, verifiable performance and raw settling speed.

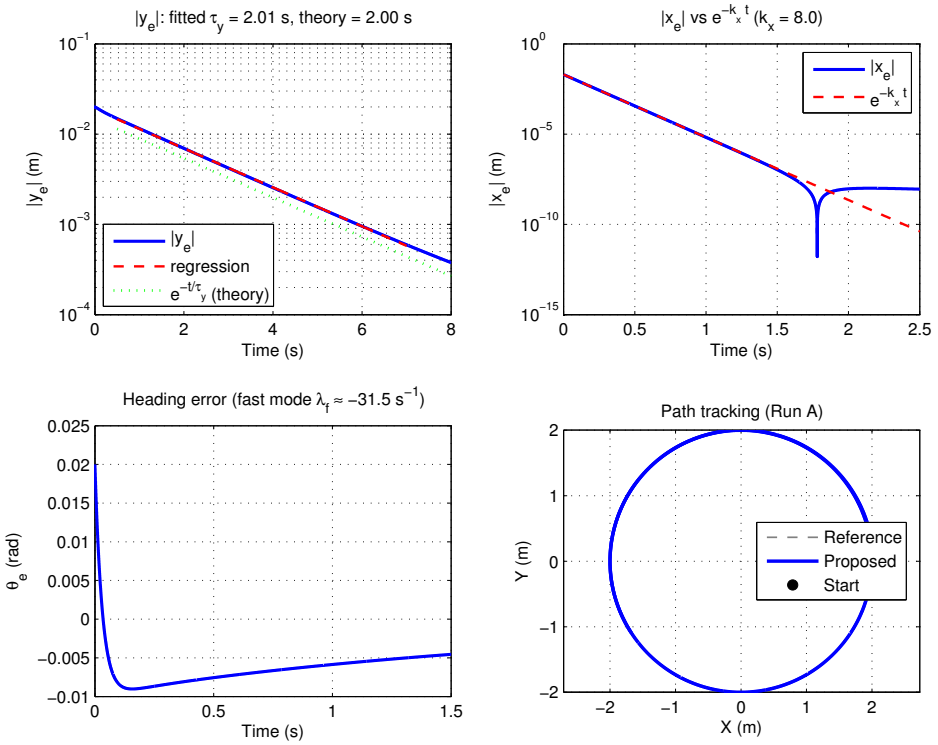


Figure 3. Case A (linear regime), proposed controller: (**a**) $|y_e|$ (semilog) with the regression line and the theoretical envelope e^{-t/τ_y}; (**b**) $|x_e|$ (semilog) versus $|x_e(0)|e^{-k_x t}$; (**c**) heading error θ_e (fast mode followed by slaving to the slow lateral mode); (**d**) path tracking.

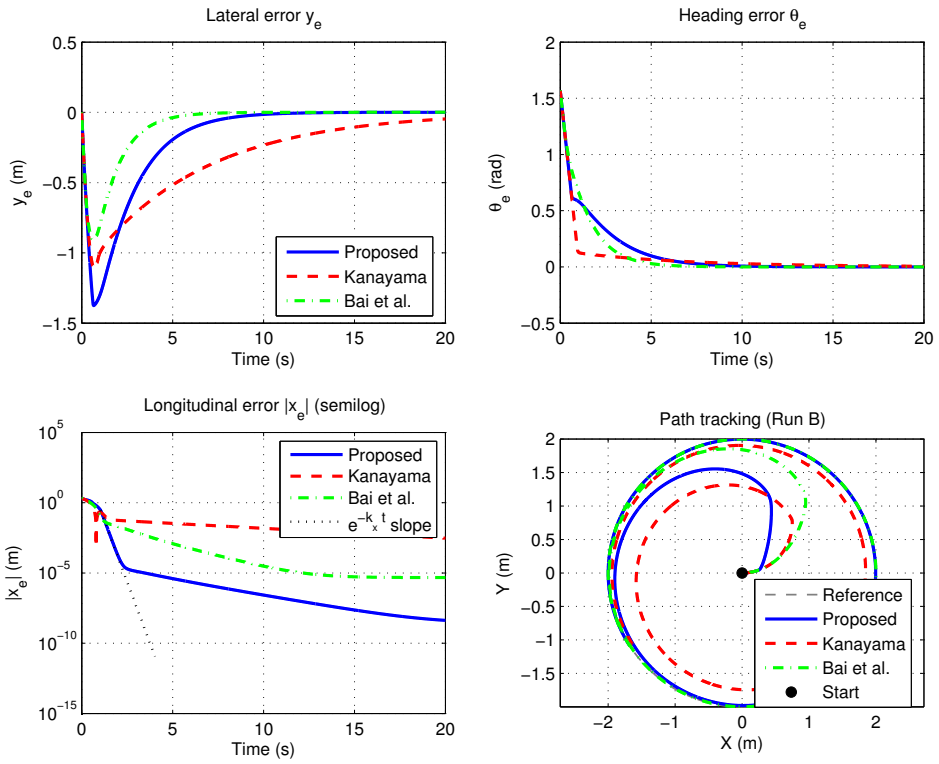


Figure 4. Case B (large initial error): (**a**) Lateral error y_e; (**b**) heading error θ_e; (**c**) longitudinal error $|x_e|$ (semilog) with the $e^{-k_x t}$ slope reference; (**d**) path tracking.

5.2. Figure-Eight Trajectory: Comparative Obstacle Avoidance

This subsection evaluates the obstacle-aware framework on a planar figure-eight reference

$$x_r(t) = a\sin(\omega_0 t), \quad y_r(t) = b\sin(2\omega_0 t), \quad \theta_r(t) = \operatorname{atan2}(\dot{y}_r, \dot{x}_r), \tag{34}$$

with $a = 2.5$ m, $b = 1.5$ m and $\omega_0 = 0.4$ rad/s (period $5\pi \approx 15.7$ s). In contrast to the circular trajectory, the reference velocities are time-varying, $v_r(t) \in [0.676, 1.562]$ m/s and $|\omega_r(t)| \le 1.472$ rad/s, so that the prescribed lateral time constant (23) varies along the path as $\tau_y(t) = k_\theta/(4k_y v_r^2(t)) \in [0.8, 4.4]$ s and the separation ratio takes values $\kappa \in [2.6, 5.9]$, satisfying the standing condition $\kappa \ge 2.5$ of Section 3.3 at every speed. The robot starts at $\mathbf{q}(0) = [1.0,\ 0.2,\ 0.5]^\mathsf{T}$, which by (3) corresponds to $x_e(0) = -0.973$ m, $y_e(0) = 0.304$ m and $\theta_e(0) = 0.376$ rad. Two obstacle scenarios are considered. Case A (single obstacle, three controllers) places one obstacle of radius $r_{\text{obs}} = 0.2$ m at $\mathbf{o} = [-1.0,\ 1.0]^\mathsf{T}$, only 0.074 m from the reference path and inside a high-curvature segment (influence-window $|\omega_r|$ up to 1.47 rad/s); this deliberately demanding placement lies outside the guideline below and serves as a stress case. The simulation horizon of Case A is $T_{\text{sim}} = 38$ s (2.4 periods); by periodicity, a third encounter would begin at ≈39.5 s, so the horizon ends shortly before it, ensuring that the final recovery of every controller—including the slowest, Kanayama+APF—completes within the recorded run. Case B (two obstacles, proposed vs. CBF-QP) follows the guideline: obstacle $\mathbf{o}_A = [2.3,\ 0]^\mathsf{T}$ ($r_{\text{obs}} = 0.2$ m, 0.20 m from the path; hard case) on the right lobe and $\mathbf{o}_B = [-2.95,\ 0]^\mathsf{T}$ ($r_{\text{obs}} = 0.25$ m, 0.45 m from the path) on the left lobe, 5.25 m apart, producing five encounter clusters over the $T_{\text{sim}} = 42$ s horizon (2.7 periods) with inter-cluster gaps of 6.3–6.5 s.

The influence radius, the obstacle positions and the actuator budget interact: trajectory tracking consumes the angular-rate budget $|\omega_r|$, and avoidance must operate on the remainder. Based on systematic placement trials, we adopt two sufficient design rules, both verified automatically before each simulation: (i) within every obstacle influence window,

$\max|\omega_r| \leq 0.5\,\omega_{\max}$, so that at least half of the angular-rate budget remains available for the avoidance correction—placements violating this rule (e.g., at the curvature extrema of the lemniscate, where $|\omega_r| \to 1.47$ rad/s) can render avoidance infeasible; (ii) obstacles are offset from the path by 0.1–0.5 m rather than centered on tangent points, where the repulsive field is nearly anti-parallel to the motion and the correction loses authority. Both obstacles in Case B satisfy rule (i) (0.61 and 0.50 rad/s against the bound 1.0 rad/s), and the initial pose is verified to lie outside all influence zones ($d_i(0) \geq d_0$), checking Assumption 5 a priori. Consistent with Remark 3, the influence radius $d_0 = 1.0$ m is chosen as the smallest value that (a) exceeds the reaction distance at the reference speed with margin, (b) yields short encounter windows (1.3–1.7 s for the proposed controller) separated by gaps of 6.3–6.5 s, so that per-encounter recovery is measurable against $3\tau_y$, and (c) remains well inside the sensing range.

All controllers use the tracking gains presented in Section 5.1 ($k_x = 8.0$, $k_y = 4.0$, $k_\theta = 32.0$); hence, the nominal recovery constants are $\tau_x = 0.125$ s and $\tau_y = 2/v_r^2(t) \in [0.8, 4.4]$ s. Additionally, all controllers are subject to the common actuator set $v \in [0.1, 1.7]$ m/s and $|\omega| \leq 2.0$ rad/s. The APF corrections use $\alpha = 5$, $\beta = 8$, $d_0 = 1.0$ m, saturated to $|\Delta v_{\text{obs}}| \leq 1.0$ m/s and $|\Delta\omega_{\text{obs}}| \leq 40$ rad/s (the latter non-binding over the operating envelope; the binding bound is the actuator limit on ω). To respect the angular-domain condition of Assumption 4, the angular correction is gated as prescribed in Section 4 with $\theta_{\text{gate}} = 1.2$ rad. The CBF-QP baseline employs $h(\mathbf{p}) = \|\mathbf{p}-\mathbf{o}\| - (r_{\text{obs}} + d_{\text{safe}})$ with $d_{\text{safe}} = 0.45$ m and $\gamma_1 = 1.2$, implemented as the analytic solution of the v-only QP, $v \leftarrow \min\{v, \gamma_1 h_i / \cos\phi_i\}$ over active obstacles with $\cos\phi_i > 0$, subject to the same saturation set; ω is not modified. The Kanayama+APF baseline augments the classic law of Section 5.1 with the same APF corrections additively, $v = v_r \cos\theta_e + k_x x_e + \Delta v_{\text{obs}}$ and $\omega = \omega_r + k_\theta \sin\theta_e + k_y v_r y_e + \Delta\omega_{\text{obs}}$; the avoidance terms therefore enter the longitudinal channel through the parasitic coupling $y_e \Delta\omega_{\text{obs}}$, in contrast to the structure-preserving design.

Beyond the per-channel metrics of Section 5.1, integrated over the full horizon, we report the per-obstacle minimum distance $d_{i,\min}$; encounter clusters (maximal intervals with $\min_i d_i(t) < d_0$); the per-cluster recovery time of y_e (last exit from the ± 0.05 m band after each cluster); the post-encounter settling time $t_s^{\text{rel}} = t_s^{y_e} - t_{\text{out}}^{\text{last}}$, which isolates recovery speed from encounter timing; the saturation occupancies; and the heading-inversion occupancy ($|\theta_e| > 2.5$ rad). The input and distance profiles of Case A are shown in Figure 5 and the two-obstacle geometry of Case B is shown in Figure 6; quantitative results are summarised in Tables 3 and 4.

Table 3. Case A (single obstacle, $T_{\text{sim}} = 38$ s): Per-channel performance; t_s = 5% settling time.

Method	Error	t_s (s)	Max $\|e\|$	ISE
Proposed SP-APF	x_e	25.46	0.974	0.288
	y_e	30.21	0.891	1.538
	θ_e	28.31	0.576	0.676
CBF-QP (v)	x_e	27.28	1.490	7.919
	y_e	31.86	1.428	8.859
	θ_e	31.68	0.633	1.807
Kanayama + APF	x_e	26.30	0.974	0.192
	y_e	35.33	0.683	2.431
	θ_e	25.23	0.613	0.468

Table 4. Obstacle avoidance summary.

Method	Case	$d_{\min}$ (m)	Recovery (s)	Post-enc. t_s	Sat. v/ω (%)	ISE
Proposed	A	0.302	4.90, 4.91	4.91	6.3/5.0	2.50
CBF-QP (v)	A	0.675	4.94, 4.96	4.96	8.9/1.2	18.59
Kanayama+APF	A	0.323	9.76, 10.03	10.03	6.2/3.9	3.09
Proposed	B	0.270 / 0.586	3.23, 2.72, 3.13, 2.72, 3.13	3.13	8.8/4.2	2.80
CBF-QP (v)	B	0.574 / 0.725	4.72, 5.11, –, 5.10, –	–	28.6/1.0	56.91

Case A (single obstacle): All three controllers are collision-free, with $d_{\min} = 0.302$ m (proposed), 0.675 m (CBF-QP) and 0.323 m (Kanayama+APF) against $r_{\text{obs}} = 0.2$ m. The CBF-QP clearance matches its certificate $r_{\text{obs}} + d_{\text{safe}} = 0.65$ m up to discretisation (Figure 5), confirming the formal invariance property; its encounter window is longer (2.6 s vs. 1.5 s) because the filter brakes earlier and exits slower—the velocity-choking signature visible in Figure 5—at the price of a longitudinal lag peaking at 1.49 m and a total ISE of 18.59, i.e., 7.4× the proposed value (2.50). The proposed controller preserves exact longitudinal decoupling during both encounters: after each cluster exits ($[8.1, 9.6]$ s and $[23.8, 25.3]$ s), $|x_e|$ resumes the $e^{-k_x t}$ decay of Figure 3 and the end-of-run residual is 3.9×10^{-5} m, while the lateral recovery completes in 4.90/4.91 s, consistent with the position-dependent constant $\tau_y(t) = 2/v_r^2(t)$ (≈4.3 s at the exit speed $v_r \approx 0.68$ m/s, below 1 s once the reference re-accelerates). Kanayama + APF deflects less ($\max|y_e| = 0.683$ vs. 0.891 m) but recovers in 9.76/10.03 s—a factor of 2 slower, in line with its 4× larger $\tau_y^{\text{Kan}} = 8/v_r^2(t)$—and its lateral error still exceeds the 0.05 m band at 35.3 s. No heading inversion occurs for any controller, and $\max_t |\theta_e| \leq 0.64 < \pi$, verifying Assumption 4 a posteriori.

The saturation occupancies in Table 4 complement this picture: the proposed controller steers (ω occupancy 5.0%) with moderate v usage (6.3%), whereas the CBF-QP filter spends its actuation budget on braking (v: 8.9%, ω: 1.2%).

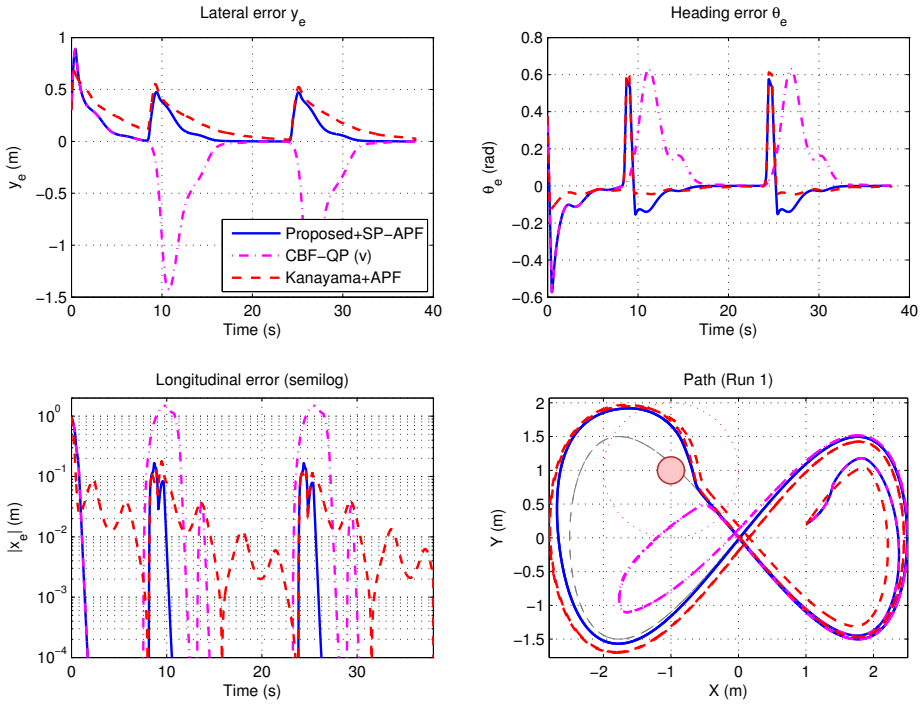


Figure 5. Case A (single obstacle): (**a**) Lateral error y_e; (**b**) heading error θ_e; (**c**) longitudinal error $|x_e|$ (semilog); (**d**) path tracking.

Case B (two obstacles): Table 4 summarises the scenario. The proposed controller maintains clearances of 0.270 m (obstacle A, margin 0.07 m over the radius) and 0.586 m (obstacle B), with per-cluster recoveries of 3.23, 2.72, 3.13, 2.72 and 3.13 s; since the inter-cluster gaps exceed $3\tau_y \approx 5$ s at the encounter speeds ($v_r \approx 1.1$ m/s), each encounter is fully absorbed before the next and no error accumulates across laps (Figure 6). All three channels settle within the horizon ($t_s = 36.09, 39.20, 39.02$ s), with end-of-run residuals of 2.5×10^{-5} m, 7.2×10^{-3} m and 2.9×10^{-3} rad.

The CBF-QP filter again provides the largest clearance (0.574 and 0.725 m) but at 56.9 total ISE (20× the proposed value 2.80) and a v-saturation occupancy of 28.6%. The clearance at obstacle A falls 0.076 m below the certificate $r_{\text{obs}} + d_{\text{safe}} = 0.65$ m: in this head-on encounter the barrier demands v below the actuator floor $v_{\min} = 0.1$ m/s, which the saturated implementation cannot honor; the margin still exceeds 2.9× the obstacle radius. More consequentially, its per-encounter recovery (4.7–5.1 s, measurable after clusters 1, 2 and 4) exceeds the windows available at the third encounter (4.0 s) and after the fifth (3.3 s), so $|y_e|$ is still 0.17 m at the end of the run and the settling times of y_e and θ_e remain undefined. Under repeated encounters, the v-only retrofit thus compounds its per-encounter accuracy deficit (ISE gap widening from 7.4× to 20×) and fails to regain nominal precision between encounters.

The v-only CBF retrofit purchases a formal forward-invariance certificate—visible in the largest clearance—at a substantial performance cost: it removes velocity authority precisely when the tracker needs it, and under repeated encounters the recovery deficit compounds. This cost is a property of the retrofit architecture rather than of CBF methodology itself: recent co-designs integrate the barrier constraint into the tracking law directly, e.g., prescribed-time tracking with a CBF safety filter for WMRs [29] and CBF-based safe tracking validated on a physical WMR [30]; combining such full-channel certificates with the structure-preserving tracker—retaining the predictable recovery constants τ_x, τ_y while gaining formal invariance—is a natural extension. Conversely, the proposed APF design offers no formal invariance guarantee: safety rests on the placement guideline, the bounded-correction analysis of Theorem 2, and a posteriori verification. The two architectures thus mark complementary points on the safety–performance spectrum that this section quantifies.

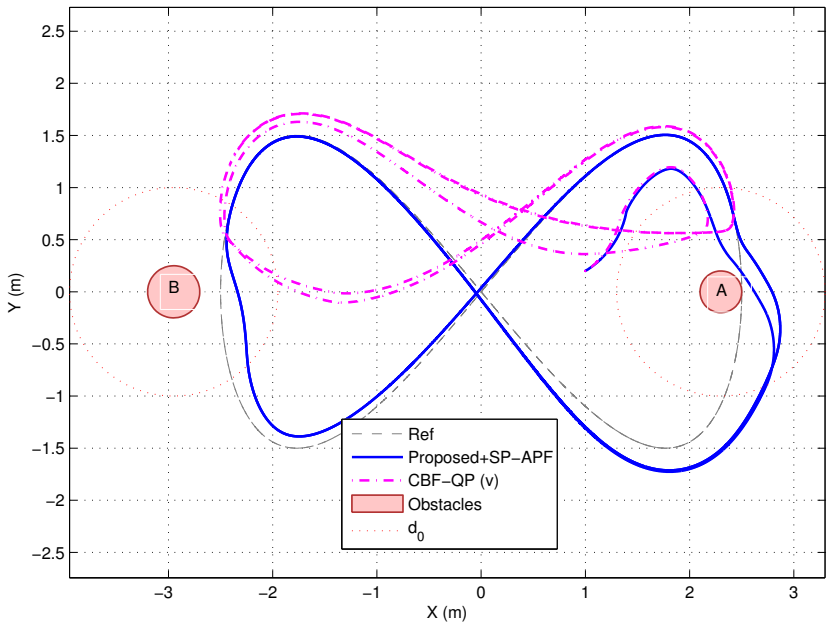


Figure 6. Case B (two obstacles): Trajectories tracking and obstacle avoidance.

6. Conclusions

This paper proposed a unified framework for trajectory tracking and static obstacle avoidance of differential-drive mobile robots. The nominal controller achieves exact longitudinal decoupling and an explicit gain-to-settling-time map, with the predicted time constants verified to within 1% in simulations. The obstacle-aware extension superimposes APF corrections in a structure-preserving manner, and a BIBS analysis with quantitative error bounds guarantees bounded deviations during avoidance and exponential recovery at the prescribed rates. Simulations on circular and figure-eight trajectories with single and multiple static obstacles, conducted at the kinematic level, confirm the predicted recovery behaviour: compared with a CBF-QP safety filter, the total ISE is reduced by factors of 7.4 and 20 in the single- and two-obstacle scenarios, and lateral recovery is twice as fast as that of a Kanayama controller augmented by APF, while operation remains collision-free with minimum clearances of 0.27–0.30 m. Future work includes experimental validation, genuinely time-varying references and dynamic-level effects (actuator dynamics, model uncertainty, wheel slip), and integration with CBF-based safety certificates.

Author Contributions: Conceptualisation, R.L. and Z.-Y.N.; methodology, R.L. and B.Z.; software, B.Z.; validation, R.L., B.Z. and Z.-Y.N.; formal analysis, R.L.; investigation, B.Z.; resources, Z.-Y.N.; writing—original draft preparation, R.L.; writing—review and editing, Z.-Y.N.; visualisation, B.Z.; supervision, Z.-Y.N.; project administration, Z.-Y.N.; funding acquisition, B.Z. and Z.-Y.N. All authors have read and agreed to the published version of the manuscript.

Funding: This research was funded by the Key Scientific Research Project Program of Universities in Henan Province under Grant 26B470009, and the National Natural Science Foundation of Fujian Province under Grant 2023J01110.

Data Availability Statement: Data are contained within the article.

Acknowledgments: The authors would like to thank the anonymous reviewers for their constructive comments that helped improve the quality of this paper.

Conflicts of Interest: The authors declare no conflicts of interest. The funders had no role in the design of the study; in the collection, analyses, or interpretation of data; in the writing of the manuscript; or in the decision to publish the results.

References

1. Siciliano, B.; Khatib, O. (Eds.) *Springer Handbook of Robotics*, 2nd ed.; Springer: Cham, Switzerland, 2016. [CrossRef]
2. Brockett, R.W. Asymptotic stability and feedback stabilization. In *Differential Geometric Control Theory*; Brockett, R.W., Millman, R.S., Sussmann, H.J., Eds.; Birkhäuser: Boston, MA, USA, 1983; pp. 181–191. [CrossRef]
3. Kolmanovsky, I.; McClamroch, N.H. Developments in nonholonomic control problems. *IEEE Control Syst.* **1995**, *15*, 20–36. [CrossRef]
4. Samson, C. Velocity and torque feedback control of a nonholonomic cart. In *Advanced Robot Control*; Canudas de Wit, C., Ed.; Springer: Berlin, Germany, 1991; Volume 162, pp. 125–151. [CrossRef]
5. Morin, P.; Samson, C. Trajectory tracking for nonholonomic vehicles. In *Robot Motion and Control: Recent Developments*; Kozlowski, K., Ed.; Springer: Berlin, Germany, 2006; Volume 335, pp. 3–23. [CrossRef]
6. Kanayama, Y.; Kimura, Y.; Miyazaki, F.; Noguchi, T. A stable tracking control method for an autonomous mobile robot. In Proceedings of the IEEE International Conference on Robotics and Automation (ICRA), Cincinnati, OH, USA, 13–18 May 1990; pp. 384–389. [CrossRef]
7. De Luca, A.; Oriolo, G. Modeling and control of nonholonomic mechanical systems. In *Kinematics and Dynamics of Multi-Body Systems*; Angeles, J., Kecskeméthy, A., Eds.; Springer: Vienna, Austria, 1995; pp. 277–342. [CrossRef]
8. Jiang, Z.P.; Nijmeijer, H. Tracking control of mobile robots: A case study in backstepping. *Automatica* **1997**, *33*, 1393–1399. [CrossRef]
9. Fierro, R.; Lewis, F.L. Control of a nonholonomic mobile robot: Backstepping kinematics into dynamics. *J. Robot. Syst.* **1997**, *14*, 149–163. [CrossRef]

10. Panteley, E.; Loría, A. On global uniform asymptotic stability of nonlinear time-varying systems in cascade. *Syst. Control Lett.* **1998**, *33*, 131–138. [CrossRef]
11. Chwa, D. Sliding-mode tracking control of nonholonomic wheeled mobile robots in polar coordinates. *IEEE Trans. Control Syst. Technol.* **2004**, *12*, 637–644. [CrossRef]
12. Zheng, Y.; Zheng, J.; Shao, K.; Zhao, H.; Xie, H.; Wang, H. Adaptive trajectory tracking control for nonholonomic wheeled mobile robots: A barrier function sliding mode approach. *IEEE/CAA J. Autom. Sin.* **2024**, *11*, 1007–1021. [CrossRef]
13. Yan, L.; Ma, B.; Jia, Y.; Jia, Y. Observer-based trajectory tracking control of nonholonomic wheeled mobile robots. *IEEE Trans. Control Syst. Technol.* **2024**, *32*, 1114–1121. [CrossRef]
14. Bechlioulis, C.P.; Rovithakis, G.A. Robust adaptive control of feedback linearizable MIMO nonlinear systems with prescribed performance. *IEEE Trans. Autom. Control* **2008**, *53*, 2090–2099. [CrossRef]
15. Dai, S.-L.; He, S.; Chen, X.; Jin, X. Adaptive leader–follower formation control of nonholonomic mobile robots with prescribed transient and steady-state performance. *IEEE Trans. Ind. Inform.* **2019**, *16*, 3662–3671. [CrossRef]
16. Chen, Z.; Tang, J.; Zuo, Z. A novel prescribed-performance path-following problem for non-holonomic vehicles. *IEEE/CAA J. Autom. Sin.* **2024**, *11*, 1476–1484. [CrossRef]
17. Li, K.; Fang, X.; Zhao, K.; Song, Y. Angle-constrained adaptive formation control with prescribed performance for multiple nonholonomic mobile robots. *IEEE Trans. Ind. Electron.* **2025**, *72*, 6307–6316. [CrossRef]
18. Khatib, O. Real-time obstacle avoidance for manipulators and mobile robots. *Int. J. Robot. Res.* **1986**, *5*, 90–98. [CrossRef]
19. Rasines, I.; Cabanes, I.; Remazeilles, A.; McIntyre, J. Robots adapting to the environment: A review on the fusion of dynamic movement primitives and artificial potential fields. *IEEE Access* **2024**, *12*, 92598–92611. [CrossRef]
20. Ames, A.D.; Xu, X.; Grizzle, J.W.; Tabuada, P. Control barrier function based quadratic programs for safety critical systems. *IEEE Trans. Autom. Control* **2017**, *62*, 3861–3876. [CrossRef]
21. Chen, Y.; Singletary, A.; Ames, A.D. Guaranteed obstacle avoidance for multi-robot operations with limited actuation: A control barrier function approach. *IEEE Control Syst. Lett.* **2021**, *5*, 127–132. [CrossRef]
22. Xie, J.; Hu, L.; Tan, Y.; Yang, J. CBF-based hierarchical quadratic programs with guaranteed feasibility for safety-critical systems. *IEEE Trans. Autom. Sci. Eng.* **2025**, *22*, 23687–23699. [CrossRef]
23. Shao, X.; Zhang, B.; Zhi, H.; Romero, J.G.; Fan, B.; Hu, Q.; Navarro-Alarcon, D. InPTC: Integrated planning and tube-following control for prescribed-time collision-free navigation of wheeled mobile robots. *IEEE/ASME Trans. Mechatron.* **2025**, *30*, 3339–3350. [CrossRef]
24. Gajbhiye, S.; Banavar, R.N. Geometric tracking control for a nonholonomic system: A spherical robot. *IFAC-PapersOnLine* **2016**, *49*, 820–825. [CrossRef]
25. Khalil, H.K. *Nonlinear Systems*, 3rd ed.; Prentice-Hall: Upper Saddle River, NJ, USA, 2002. Available online: https://www.pearson.com/ (accessed on 15 March 2026).
26. Kokotović, P.; Khalil, H.K.; O'Reilly, J. *Singular Perturbation Methods in Control: Analysis and Design*; SIAM: Philadelphia, PA, USA, 1999. [CrossRef]
27. Bacciotti, A.; Mazzi, L. A necessary and sufficient condition for bounded-input bounded-state stability of nonlinear systems. *SIAM J. Control Optim.* **2000**, *39*, 478–491. [CrossRef]
28. Bai, J.; Du, J.; Li, T.; Chen, Y. Trajectory tracking control for wheeled mobile robots with kinematic parameter uncertainty. *Int. J. Control Autom. Syst.* **2022**, *20*, 1632–1639. [CrossRef]
29. Alavi Nasab, A.; Badiei, R.; Asemani, M.H. Safe prescribed time controller for wheeled mobile robots by using control barrier functions as a safety filter. *ISA Trans.* **2025**, *162*, 119–133. [CrossRef]
30. Rehman, I.U.; Abadi, A.; Labbadi, M.; Lew Yan Voon, L. Robust and safe control of mobile robots using control barrier functions: Experimental results. *Eur. J. Control* **2026**, *91*, 101621. [CrossRef]

Disclaimer/Publisher's Note: The statements, opinions and data contained in all publications are solely those of the individual author(s) and contributor(s) and not of MDPI and/or the editor(s). MDPI and/or the editor(s) disclaim responsibility for any injury to people or property resulting from any ideas, methods, instructions or products referred to in the content.